NATIONAL BUREAU OF STANDARDS REPORT

10 071

INFRARED REFLECTANCE MEASUREMENTS

Final Report to the
National Aeronautics and Space Administration
Order Number R-09-022-032
and
Order Number L-80,662

NBS

U.S. DEPARTMENT OF COMMERCE
NATIONAL BUREAU OF STANDARDS

14

NATIONAL BUREAU OF STANDARDS REPORT

NBS PROJECT		NBS REPORT
2210484	January 1, 1967 – June 30, 1969	10 071

INFRARED REFLECTANCE MEASUREMENTS

by
Joseph C. Richmond
Jon C. Geist

Final Report to the
National Aeronautics and Space Administration
Order Number R–09–022–032
and
Order Number L–80,662

U.S. DEPARTMENT OF COMMERCE
NATIONAL BUREAU OF STANDARDS

TABLE OF CONTENTS

	Page
1. Introduction	1
2. The Ellipsoidal Mirror Reflectometer	1
2.1 Background	1
2.2 Current Work	3
2.2.1 Flux Averaging Devices	6
2.2.1.1 Averaging Spheres	7
2.2.1.2 Large Metal Strip Bolometers	18
2.2.1.3 Mechanical Scanning	19
2.2.2 Inverse Mode Operation	29
2.2.2.1 Theory of Operation	29
2.2.2.2 Experimental Results	34
3. The Interferometer Spectrometer	34
3.1 Background and Theory	34
3.2 Description of the Block Interferometer	40
3.3 Interface Problems	42
3.4 Computer Code for Data Reduction	43
3.5 Tests of Interferometer Spectrometer	46
3.5.1 Wavelength Calibration	46
3.5.2 Angular Sensitivity	47
3.5.3 Strong Reflectometer	48
4. Summary	54
5. References	55
6. Appendix A	57
7. Figures	64

LIST OF ILLUSTRATIONS

		Page
1.	Schematic diagrams of ellipsoidal mirror reflectometer. A - direct mode. B - inverse mode.	63a
2.	Spectral directional-hemispherical reflectance of mu sulfur.	64
3.	Spectral directional-hemispherical reflectance of cesium iodide powder.	65
4.	Spectral directional-hemispherical reflectance of cesium iodide powder.	66
5.	Spectral directional-hemispherical reflectance of a sprayed sodium chloride coating.	67a
6.	Spectral directional-hemispherical reflectance of gold-coated No. 600 silicon carbide polishing paper.	68
7.	Parameters used in deriving scanning equations.	69
8.	Ideal raster pattern for scanning.	70
9.	Schematic of scanning system and pattern produced. The two scan patterns are superimposed.	71
10.	Block diagram of signal processing system used with scanner.	72
11.	Block diagram of equipment used to test reproducibility of integrator, and results obtained.	73
12.	Block diagram of equipment used to test reproducibility of amplifier and detector, and results obtained.	74
13.	Block diagram of equipment used to test reproducibility of scanner, and results obtained.	75
14.	Block diagram of equipment used to test reproducibility of Globar source, and results obtained.	76
15.	Sketch showing relative size of scan pattern, images (1 and 2) and detector, and results obtained.	77
16.	Cross-sectional drawing of interferometer head. M_1 is the movable mirror, M_2 the fixed mirror, S the beamsplitter, C the compensator plate, e_1 the entrance aperture and e_2 the exit aperture.	78

LIST OF ILLUSTRATIONS (cont'd.)

		Page
17.	Plot of mirror motion during a sweep. T is sweep time, F is fly-back time, R is recovery time and B/2 is excursion, or maximum distance of travel of the mirror.	78
18.	A typical interferogram for a polychromatic beam. Only the central 180 points of the 521 recorded are included on this plot.	79a
19.	Block diagram of the electronic system of the interferometer spectrometer.	80
20.	Normalized detector response as a function of detector position along a horizontal line through the optical axis 28 inches from the interferometer-source combination. Distances are in inches, with positive distances to the right and negative distances to the left of the optical axis, facing the interferometer.	81a
21.	Normalized detector response as a function of detector position along a vertical line through the optical axis, 28 inches from the interferometer-source combination. Distances are in inches, with positive distances above and negative distances below the optical axis.	82a
22.	Optical diagram of the Strong reflectometer used with the interferometer spectrometer.	83
23.	Typical curves produced by analog reduction of an interferogram recorded without background subtracted (lower curve) and with background subtracted (upper curve).	84a
24.	Typical spectrum produced by a Globar source in purified atmosphere (top curve) and ambient atmosphere (middle curve). The difference, bottom curve, represents the observed absorption of the ambient atmosphere.	85a
25.	Typical spectral distribution of observed atmospheric absorptance, obtained by digital reduction of interferograms. Each point is the ratio of the difference in observed spectral radiances of the Globar source observed in purified and ambient atmospheres to that in the purified atmosphere.	86a
A1.	Ellipsoidal mirror reflectometer in direct mode, showing parameters used in equations A3 through A8.	87a
A2.	Ellipsoidal mirror reflectometer in inverse mode, showing parameters used in equations A11 through A16.	88a

1. Introduction

This is the final report on work done under NASA contracts R-09-022-032 and L-80-622.

The contracts called for work to be done in four specific areas: 1) continued development of the ellipsoidal mirror reflectometer, 2) an investigation of the suitability of the interferometer spectrometer for thermal radiation property evaluations, 3) a study of the relation of surface roughness to the geometric distribution of radiant energy reflected from the surface, and 4) development of standards of solar reflectance.

Because of the deobligation of funds, no work was done on categories 3 and 4 above. This report covers work done on (1) further development of the ellipsoidal mirror reflectometer and (2) with the interferometer spectrometer.

2. The Ellipsoidal Mirror Reflectometer

2.1 Background

The original concept of the ellipsoidal mirror reflectometer was developed in 1959 [1] and an instrument embodying this concept was constructed in 1960. The basic concept is to use a portion of a prolate ellipsoid, cut normal to the principal axis, and extending from the apex to or beyond the first focal plane, to collect the radiant energy reflected by a specimen at the first focal point and focus it onto a detector at the second focal point. The specimen is irradiated by a narrow beam of monochromatic radiant energy, which passes through a small hole in the ellipsoidal mirror. If an ellipsoid of appreciable eccentricity is used, the first and second focal points will be separated by an appreciable

distance, and the specimen can be heated or cooled without directly affecting the detector.

The initial model of this reflectometer was constructed in 1960. The mirror was about 32 cm in diameter, and the distance between the two focal planes was about 43 cm. An elliptical hole about 25 mm by 19 mm in size was centered on a line passing through the first focal point at an angle of 7° to the major axis of the ellipsoid. A Golay cell of large sensitive area was used as the detector at the second focal point. The detector proved to be highly microphonic, and in spite of elaborate precautions to isolate the detector from air-borne and structure-borne noise, usable signal-to-noise ratios were not obtained. Work on this instrument for the years 1962 through 1964 is reported in NBS Technical Notes 252 [2] and 267 [3].

The Golay cell was shown to be definitely unsuitable for use with this instrument, and a large-area thermopile detector, procured to replace the Golay cell, was shown to have serious variations in sensitivity with the location on the sensitive area of the detector of a small beam of incident radiant energy, and with the angle of incidence of the incident radiant energy. The use of several different diffusing devices to reduce the effect of these variations in sensitivity was studied.

During the 1965 contract year the instrument was further developed [4,5], and its wavelength range extended to about 7 μm. The principal improvements were the use of a sulfur-coated averaging sphere as a flux-averaging device for the thermopile detector, and the use of shields in

the first focal plane of the ellipsoid to quantitatively evaluate the geometric distribution of flux reflected by a specimen, so that accurate corrections could be made for known flux losses. Results were shown to be accurate to better than two percent of the measured reflectance.

The wavelength limitation was due to low signal-to-noise ratios at longer wavelengths. Preliminary studies were made of the feasibility of using an interferometer spectrometer for reflectance measurements. Under certain circumstances this instrument has the capability of increasing the signal-to-noise ratio by several orders of magnitude over that observed with conventional dispersion spectrometers.

2.2 Current Work

Current work with the ellipsoidal mirror reflectometer has been concentrated along several different lines. The major problems involved in making accurate reflectance measurements at long wavelengths with the ellipsoidal mirror reflectometer are related to the difficulty in obtaining satisfactory signal-to-noise ratios, which are in turn related to the optical properties of the ellipsoid. A reflectance measurement necessarily involves separate evaluations of incident and reflected flux.

In a true ellipsoidal mirror all photons leaving the first focal point will be reflected by the mirror in a direction such that they will pass through the second focal point. The photons leaving a point p in the first focal plane at some distance from the first focal point will not pass through a single point in the second focal plane, but will be confined to a roughly elliptical area with its major axis along a line

through the second focal point. The size and eccentricity of this elliptical area is determined both by the eccentricity of the ellipsoid and the distance from point p to the first focal point. The linear magnification factor, m, of the mirror will vary with the position, x, on the mirror from which the ray from point p is reflected toward the second focal plane. If s is the distance from the point p to point x on the mirror, and s' is the distance from point x to point p' where the ray crosses the second focal plane, $m = s'/s$. For points near the first focal point, the distance s is closely approximated by the distance from the first focal point to x, and s' by the distance from x to the second focal point. The magnification m will be at a maximum when x is at the apex of the ellipsoid, and will decrease with the distance from the apex to x.

In the partial ellipsoid used in this work, if optically perfect, the value for m with x at the apex is computed to be approximately 5.69, and with x at the rim the corresponding value is approximately 2.96. As a result a sharply defined area of uniform radiance in the first focal plane surrounding the first focal point will form an enlarged image surrounding the second focal point in the second focal plane. However, the irradiance on this image will not be uniform. It can be thought of as being made up by superimposing an infinite number of images, each of which is uniform in irradiance, and which is formed by the rays striking points x that are equally distant from the apex of the ellipsoid. Such a composite image will be uniform in irradiance over the central area corresponding to the image with the smallest magnification factor, 2.96, and the irradiance

will decrease monotonically to a minimum at the edge, which will be that of the image with the largest magnification factor, 5.69.

Actually the image will be somewhat more blurred than is indicated above for a perfect ellipsoid, because the ellipsoid used is not perfect. This results in a slightly larger image with somewhat greater blurring than is indicated above. Also, in any real case, the irradiated area on a real specimen in the first focal plane will not be uniform in radiance, but will vary in radiance with direction, and the irradiance distribution over the enlarged image will vary with this directional variation in radiance of the specimen.

It has been shown in previous reports [3,5] that the thermopile detector used in this work varied significantly in response with the location of a small irradiated area on the sensitive area of the detector, and with direction of incidence of the incident flux. Obviously such a detector would not have the same response to the small-area small-solid-angle beam incident on the specimen and the large-area large-solid-angle beam focused on the detector by the ellipsoidal mirror. Identical response would not even be expected when a mirror at the first focal point is used to evaluate the incident flux. It is thus necessary to use a flux averaging device if the reflectometer is to give accurate results when used in the normal mode.

An alternative approach is to use the instrument in the inverse mode. The two modes are illustrated in figure 1. In the direct mode, figure 1a, the sample is irradiated by a small diameter monochromatic beam of small

solid angle, and the flux reflected by the specimen is collected by the ellipsoidal mirror and focused onto a detector at the second focal point. In the inverse mode a large area source of uniform radiance is located at the second focal point of the ellipsoid, and the radiant energy from the source is collected by the ellipsoid and focused onto the specimen, which is uniformly irradiated over a hemisphere. The flux reflected by the specimen into a small solid angle is directed through a monochromator to a detector.

2.2.1 Flux Averaging Devices

There are three basic requirements for the detector system to be used with the ellipsoidal mirror reflectometer. First, the system, detector plus diffuser, should show no angular sensitivity--that is, the sensitivity should be independent of the angle of incident flux over the range of 0° to 25° from the normal. Second, the system should show no areal sensitivity--that is, the sensitivity should be independent of the size, shape or location of the irradiated area, so long as all of the flux strikes the sensitive area. Third, the overall sensivity of the system must be high enough to permit accurate measurements to be made with a conventional infrared source such as a Globar, a conventional monochromator, and an optical system with a relatively small numerical aperture.

An averaging sphere coated with pressed mu sulfur was used as the flux averaging device in the earlier work. With this averaging sphere

satisfactory signal-to-noise ratios were obtained at wavelengths out to about 7 μm. The desired range of the instrument is to at least 15 μm, and preferably to 25 μm or beyond. In order to increase the usable range of the instrument to longer wavelengths, it was necessary to develop a more efficient flux averaging device, either by increasing the efficiency of the averaging sphere or by other means.

2.2.1.1 Averaging Spheres

An averaging sphere is simpler than the integrating sphere of a reflectometer. It has only two apertures, an entrance aperture and a detector aperture. The entire remaining interior surface of the sphere has the same high reflectance, ρ_w.

The areas of interest are A, the total area of the sphere wall, openings included; A_e, the area of the entrance port; A_D, the area of the detector port; A_v, the area viewed by the detector; and A_i, the area irradiated by the incident beam. The size of A_i, the area irradiated by the incident beam, will vary with the beam geometry, and hence should not appear in the equations, since the purpose of the averaging sphere is to eliminate the effects of beam geometry on the magnitude of the signal produced by the detector.

While A_i does not appear in the equations, its location and maximum size are important in the design of an averaging sphere. It is obvious

that A_i should never include the detector aperture, A_D; otherwise the detector might be directly irradiated by part of the incident beam. If the effects of beam geometry are to be eliminated, one of two basic designs must be used. In the first design, A_v never includes any part of A_i. Hence any flux reaching the detector must be reflected at least twice by the sphere wall. This is the design that was used with the ellipsoidal mirror reflectometer. In the second design, A_v always includes all of A_i, and a major portion of the flux will reach the detector after only one reflection from the sphere wall. The mathematical treatment for the two designs is different.

The derivation of the equations is based on certain assumptions. These are (1) that the sphere surface has perfectly diffuse uniform reflectance ρ_w; (2) that none of the flux passing out of the apertures is returned to the sphere; and (3) that none of the flux passing out the detector aperture from areas of the sphere wall other than A_v reaches the detector. With these assumptions, we can proceed to derive the equations relating the incident flux, Φ_o, to that viewed by the detector, Φ_D.

Let us first consider the case where A_v and A_i are mutually exclusive. The flux Φ_o is reflected by the area A_i, and the fraction $\Phi_o\rho_w$ is uniformly distributed over the entire surface of the sphere. This is true regardless of the size or shape of A_i--the only requirements are that the area A_i have perfectly diffuse reflectance and that the reflectance ρ_w be uniform over the area A_i. The fraction A_v/A of the flux $\Phi_o\rho_w$ will be incident

on the area A_v, and of this the fraction $\rho_w A_D/A$ will reach the detector.[1] Hence the fraction Φ'_D of the flux that reaches the detector after the first reflection from A_v (twice reflected by the sphere wall, once from A_i and once from A_v) will be

$$\Phi'_D = \Phi_o \rho_w^2 A_v A_D / A^2 \qquad (1)$$

Of the flux reflected once by A_i, the fractions A_D/A and A_e/A will be lost out the detector and entrance apertures, and the remainder $\Phi_o \rho_w [1 - (A_D + A_e)/A]$ will be reflected by the sphere wall, and the fraction $\rho_w A_v/A$ will be incident on the area A_v, of which $\rho_w A_D/A$ will reach the detector. Hence Φ''_D, the flux reaching the detector from A_v, after the third reflection (once from A_i, once from A and once from A_v) will be

$$\Phi''_D = \Phi_o \rho_w^3 A_v A_D / A^2 \, [1 - (A_D + A_e)/A] \qquad (2)$$

and after the fourth reflection (once from A_i, twice from A and once from A_v)

$$\Phi'''_D = \Phi_o \rho_w^4 \frac{A_v A_D}{A^2} \left[1 - \frac{A_D + A_e}{A}\right]^2 \qquad (3)$$

1/ The use of the ratio A_D/A is based on the assumption that all of the flux from A_v that passes out the detector aperture reaches the detector. This may not be true with some designs, particularly if the area of the detector aperture is larger than the sensitive area of the detector. If this is the case, the diffuse configuration factor from area A_v to the sensitive area of the detector, $f_{A_v\text{-}D}$, should be substituted for the fraction A_D/A.

and so forth.

Summing the terms after many reflections, we get

$$\Phi_D = \Phi_o \rho_w^2 \frac{A_v A_D}{A^2} \frac{1}{1 - \left(1 - \frac{A_D + A_e}{A}\right)\rho_w} \tag{4}$$

which can be rewritten as

$$\Phi_D = \frac{\Phi_o \rho_w^2 A_v A_D}{A[A - \rho_w(A - A_e - A_D)]} .$$

For the case where A_v always includes all of A_i, the equation is slightly different. In this case, on the first reflection from A_i, the fraction $\Phi_o \rho_w$ of the incident flux will be reflected and distributed uniformly over the entire sphere wall, and of this the fraction A_D/A will reach the detector. Hence,

$$\Phi'_D = \Phi_o \rho_w A_D / A. \tag{5}$$

Of the flux $\Phi_o \rho_w$ reflected from A_i, the fraction A_v/A will be incident on area A_v, and of this the fraction $\rho_w A_D/A$ will reach the detector. Hence,

$$\Phi''_D = \Phi_o \rho_w^2 \frac{A_v A_D}{A^2} \tag{6}$$

Of the flux $\Phi_o \rho_w$ reflected initially from A_i, the fractions A_D/A and

A_e/A will be lost, and $1 - (A_D + A_e)/A$ will be reflected a second time, of which the fraction A_v/A will reach area A_v, and of this the fraction $\rho_w A_D/A$ will reach the detector. Hence,

$$\Phi_D'''' = \Phi_o \rho_w^3 \frac{A_v A_D}{A^2} \left(1 - \frac{A_D + A_e}{A}\right) \tag{7}$$

and

$$\Phi_D'''''' = \Phi_o \rho_w^4 \frac{A_v A_D}{A^2} \left[1 - \left[\frac{A_D + A_e}{A}\right]^2\right] \tag{8}$$

Summing after many reflections, we get

$$\Phi_D = \Phi_o \rho_w \frac{A_D}{A} + \Phi_o \rho_w^2 \frac{A_v A_D}{A^2} \left[\frac{1}{1 - \left(1 - \frac{A_D + A_e}{A}\right)\rho_w}\right] \tag{9}$$

which can be rewritten as

$$\Phi_D = \Phi_o \rho_w \frac{A_D}{A} \left[1 + \frac{\rho_w A_v}{[A - \rho_w (A - A_D - A_e)]}\right]$$

The only difference in the two equations is the first term in equation (9), which does not appear in equation (4).

An examination of equation (4) indicates that this type of averaging sphere has a very low efficiency, which can be expressed

as the ratio Φ_D/Φ_o. Because of physical limitations, particularly the requirement that A_v include neither A_D or A_i, A_v/A generally does not exceed about 0.2. A_e/A and A_D/A are generally about 0.035. The reflectance of the wall, ρ_w, varies with wavelength, but a representative value for sulfur is 0.9. When these values are substituted in equation (4), $\Phi_D/\Phi_o = 0.033$, a rather low number. It is physically not possible to increase Φ_D/Φ_o substantially by changing the parameters of the averaging sphere.

While the above analysis indicates that the averaging sphere does not offer great promise of being useful over the entire range of wavelengths at which it is desired to make measurements, it was considered desirable to attempt further improvements in the design or sphere coating to extend its range as much as possible. The convenience of the averaging sphere makes it extremely useful in the wavelength range where it is applicable.

Three types of improvements to the averaging sphere have been considered. The first is a design change in the averaging sphere in which the detector is a thermopile that forms the interior surface of half or more of the averaging sphere. The area viewed by the detector, A_v, would be coated with a diffusely reflecting high reflectance coating. The maximum theoretical efficiency of such a system would be achieved if A_e/A is small, let us estimate 0.1, and A_D and A_v are each half of the remaining area of the sphere, or A_D/A and A_v/A have a value of 0.45 each. Substituting these values, and 0.9 for ρ_w, into equation (9) gives $\Phi_D/\Phi_o = 0.73$. This design apparently offers appreciable advantages over that in which

A_v and A_i are mutually exclusive. The efficiency of a system of this design will approach 1.0 as ρ_w approaches 1.0 and A_e approaches zero.

While a system of this type offers many theoretical advantages, its construction would be difficult. There is no thermopile detector available commercially that has a hemispherical receiving surface, and construction of such a detector would be expensive. In addition, in order to obtain high sensitivity and short time response, it is necessary to operate a thermopile in vacuum, which would necessitate evacuating the entire diffusing sphere. For these reasons, this approach was abandoned.

Equation (4) shows that the efficiency of an averaging sphere varies as the square of the reflectance of the sphere coating. The reflectance of mu sulfur is shown in figure 2. The reflectance drops below 0.9 at about 5.5 μm, and below 0.8 at about 6.8 μm. The longest wavelength at which a satisfactory signal-to-noise ratio was obtained with the sulfur coated sphere was 7.0 μm, where the reflectance of the sulfur was about 0.75. The efficiency of an averaging sphere at long wavelengths could be increased significantly by use of a diffusely reflecting coating having high reflectance. The second approach was therefore to try to find a diffusely reflecting sphere coating with high reflectance at long wavelengths. Most diffusely reflecting coatings reflect by body scattering. Body scattering is produced as a result of refraction and reflection of photons at grain boundaries in a polyphase matrix. It has been shown [6] that the reflectance of a body-scattering material is related to the parameter β

$$\beta = \sqrt{\frac{K}{(K + 2S)}} = \sqrt{\frac{K/S}{K/S + 2}} \qquad (10)$$

where K is the absorption coefficient and S is the scattering coefficient. The reflectivity ρ_∞ is given by

$$\rho_\infty = \frac{1-\beta}{1+\beta} \qquad (11)$$

which shows that a low value of β is required for high reflectance. The value of β is determined by the ratio of the absorption coefficient K to the scattering coefficient, S, as is shown in equation (10) and not by the absolute magnitude of either coefficient.

The absorption coefficient, K, is a function of chemical composition, and cannot readily be altered for any given material. The scattering coefficient, S, on the other hand, is strongly dependent on the microstructure of the material. For a powder, S is a function of index of refraction, particle size, particle size distribution and packing. The amount of scattering is roughly proportional to the particle surface area per unit volume of powder, and hence increases as the average particle size decreases, until the particles get to a size where the type of scattering changes from Mie scattering to Rayleigh scattering, which occurs as the particle diameter becomes appreciably smaller than the wavelength of the light being reflected. Frustrated internal reflection [7] occurs as the scattering particles approach each other to within a distance that is less than the wavelength of the light involved, and reduces the amount of reflection and refraction at the interface. As a

result, increasing the density of a powder beyond a certain value will decrease the scattering coefficient. The most highly reflecting powders are light and fluffy.

A brief survey was made of materials that might be suitable for use as a sphere coating, and BaF_2, CaF_2, LiF, CsI, MgF_2, NaF, AlF, and NaCl were selected for preliminary tests. The reflectance of a layer of powder about 4 mm thick was measured with the Cary-White 90 reflectometer. Only CsI and NaCl showed promise of approaching mu sulfur as a sphere coating.

High purity cesium iodide powder had high reflectance over the entire wavelength range of 2.5 to 22.5 μm, as shown in figures 3 and 4, and as reported in reference 8. However, the high-purity cesium iodide is expensive ($5.00 per gram) and poisonous, and no attempts were made to prepare coatings from it.

A technique was developed for preparing coatings of sodium chloride that had high reflectance at wavelengths out to about 10 μm, except for an absorption band near 3 μm, and were near-perfect diffusers. A spectral reflectance curve for a typical sample of sodium chloride is shown in figure 5.

The process of applying the sodium chloride coating is described in reference 9 as Appendix A. Reagent grade NaCl was suspended in absolute ethyl alcohol by grinding in a ball mill for 48 hours. A charge consisted of about 1350 grams of NaCl and one liter of alcohol in a one-gallon porcelain lined ball mill filled about 3/4 full of 1-inch

diameter porcelain balls. The mixture was ground for 48 hours, after which the suspension was separated from the balls and stored in sealed glass containers. When allowed to stand for 30 minutes the NaCl particles would partially settle out, leaving about an inch of clear liquid at the top of a full 1-gallon glass jar. This provided a quick check as to the proper content of alcohol in the mixture.

The suspension was sprayed with an industrial-type spray gun, at an air pressure of about 30 psi. The spray gun was adjusted to give good atomization, and to produce a wet coating. Best results were obtained by moving the gun over the surface, at a distance of about 30 cm, with the spray directed approximately normal to the surface being sprayed, and with constant motion of the gun in a raster pattern over the surface. If too much NaCl was applied to one spot at one time, the coating slumped, and had to be removed. Frequent agitation of the mixture was required to keep the NaCl in suspension. On the order of 30 to 50 thin applications, with partial drying between coats, was required to build up the desired thickness, which was about 3 mm, required to develop the maximum reflectance. Best results were obtained when the previous coat was still slightly damp when the next coat was applied. When a rough surface resulted from improper adjustment of the spray gun or improper spraying technique, it was smoothed while still slightly damp. This was done with a piece of glass ground to the desired contour of the coating. Rough surfaces had lower reflect-

ance than smooth surfaces, and were less diffuse.

The NaCl suspension was very corrosive on spray gun parts, and a special spray gun was used in which all parts that came in contact with the sprayed suspension were made of corrsion-resisting steel or plastic. When the coating was applied to metals that were subject to corrosion, including some stainless steels, corrosion products, formed at the coating-metal interface, diffused into the coating and reduced its reflectance. This could be prevented by applyi. · a coating of corrosion resisting and alcohol-resisting paint to the metal before applying the sodium chloride coating. White epoxy paint was found suitable for this purpose.

The secret of producing high-reflectance coatings was to start with high-purity materials, and maintain absolute cleanliness in every step of the operation. The ball mill used was especially cleaned, and used only for the sodium chloride coating. Care was taken to avoid deposition of dust and dirt during the spraying operation.

The sodium chloride coating produced by the above procedure had reasonably good mechanical properties. Apparently there was sufficient solubility of the NaCl in the alcohol to produce adequate binding together of the particles on evaporation of the alcohol. The coating was soft, but not excessively so, having a texture similar to ordinary chalk. It was considerably harder and more durable than a smoked magnesium oxide coating.

There was no evidence of deterioration of the coating due to absorption of moisture in the ordinary laboratory atmosphere at about 50% relative

humidity for a period of several months.

The third approach to improving the efficiency of the integrating sphere was to roughen the interior surface of the sphere to diffuse the reflected flux, and to apply over the roughened substrate a layer of vacuum deposited gold to produce the high reflectance. Sandblasted or shot blasted surfaces were found to be rather poor diffusers. A surface was prepared by the Texas Instrument Company by electrodepositing copper at high current densities. Such a surface was a relatively good diffuser on a macro scale, and was suitable for use in a large integrating sphere, but the individual crystal faces making up the surface were so large that a small diameter laser beam was reflected as a shotgun pattern of bright spots.

The best metallic diffusing surface was produced by V. R. Wiedner of NBS, who had vacuum deposited gold applied to a sample of No. 600 silicon carbide metallographic polishing paper. Figure 6 is a reflectance curve of this material. It proved to be a reasonably good diffuser at all wavelengths in the 2.5 to 22.5 μm range, and had high reflectance over this entire range. However, it was not easy to construct an averaging sphere of this material.

2.2.1.2 Large Metal Strip Bolometers

Another possibility is a large metal strip bolometer. Blevins [10] has shown that such a detector is essentially free from variations in sensitivity with area irradiated and with angle of

incidence, provided the irradiated area is kept away from the edges. His tests showed that when about 80% of the area of a detector was used, the errors due to variations in areal and angular sensitivity did not exceed 2% of the measured value.

Three metal strip bolometers were constructed, and sent to the NBS shops for coating. Unfortunately, satisfactory coatings were not obtained. Further work on this approach was curtailed by lack of funds.

2.2.1.3 Mechanical Scanning

An alternative to using an optical averaging device to compare images of different sizes and different flux density distributions is to use mechanical scanning combined with electronic integration of the signal produced by the detector.

It is easy to see intuitively that the total signal produced when an image is scanned over the surface of a detector in a raster pattern will be proportional to the total flux in the image. Assume that the detector is made up of a large number of small square or rectangular areas, and that the image is also made up of some other number of similar areas. If we then move the detector so that each area on the detector samples each area on the image once only, we can see that the sum of the signals produced will be the same, regardless of the size or flux distribution in the image, provided only that the areas chosen are of such a size that the sensitivity of the detector is uniform over each small area, or the flux distribution in the image is uniform over each small area. Only one of these two conditions need be satisfied for the system to work. However, it is necessary for each area on the detector to sample every area of the image, which means that the raster pattern of movement of the detector must be such that the horizontal sweeps extend beyond the edges of the image on both sides, by at least the width of the detector, and that the first sweep include the top of the image in no more than the bottom row of areas on the detector, and that the last

sweep include the bottom of the image in no more than the top row of areas on the detector. No harm is done if the size of the raster pattern exceeds these minimum dimensions. The vertical dimension of the individual areas on the detector and image is ΔS, the spacing of the raster pattern, and the horizontal dimension is the distance traveled by the detector in one cycle of the chopper.

The validity of the above theorem can be shown mathematically for a single sweep, based on the assumption that the raster spacing, ΔS, is small enough that there is no significant variation in detector sensitivity or image irradiance in the vertical direction. The horizontal variation in sensitivity of the detector is represented by $A(x')$ (figure 7) and the horizontal variation in irradiance of the image by $B(x)$. The width of the detector is a, and that of the image, b. The position of the detector during a scan is represented by t, x' represents a point on the detector, and x a point on the image. Under these conditions, the signal I_t from the detector at any particular position t of the detector will be represented by

$$I_t = \int_{x=o}^{t} A(x')\, B(x)\, dx \,, \qquad (12)$$

where $x' = x+a-t$ and the total integrated signal, I, for one entire sweep,

by

$$I = \int_{t=o}^{a+b} \left[\int_{x=o}^{t} A(x')\, B(x)\, dx \right] dt \qquad (13)$$

where $x = t-a+x'$.

Since $A(x') = o$ for $x' < o$, this becomes

$$I = \int_{t=o}^{a+b} \left[\int_{x=t-a}^{t} A(x')\, B(x)\, dx \right] dt. \qquad (14)$$

Since $dx = dx'$

$$I = \int_{t=o}^{a+b} \left[\int_{x'=o}^{a} A(x')\, B(x'+t-a)\, dx' \right] dt. \qquad (15)$$

By changing the order of integration

$$I = \int_{x'=o}^{a} A(x') \left[\int_{t=o}^{a+b} B(x'+t-a)\, dt \right] dx' \qquad (16)$$

Since $dt = dx$

$$I = \int_{x'=o}^{a} A(x') \int_{-a+x'}^{b+x'} B(x)\, dx\, dx'. \qquad (17)$$

Since there is no contribution to the integral for $x<o$, $b<x$, and $o \leq x' \leq a$, this becomes

$$I = \int_{x'=o}^{a} A(x') \int_{x=o}^{b} B(x)\, dx\, dx' \qquad (18)$$

which can be rewritten

$$I = \int_{x'=o}^{a} A(x')dx' \int_{x=o}^{b} B(x)\, dx. \qquad (19)$$

Equation (19) says in essence that the total integrated signal from the detector during a sweep is the integrated sensitivity of the detector, represented by the first integral, times the integrated irradiance of the image, represented by the second integral, and is independent of the sensitivity distribution of the detector and the irradiance distribution of the image.

A similar theorem has been proved for the two-dimensional case [11], but there is no physical scanning system that can rigorously produce a two-dimensional integration, which would require scanning in two directions simultaneously. However, in the limit as ΔS approaches zero (see figure 8)

$$\lim_{\Delta S \to o} I = \left[\int_{y=o}^{b} \int_{x=o}^{a} A(x'y')\, dx'\, dy' \right] \times \left[\int_{y=o}^{d} \int_{x=o}^{c} B(xy)\, dx\, dy \right] \qquad (20)$$

In the real case, where ΔS is finite, equation (20) is valid to the extent that the conditions mentioned above are met, namely that there is either no significant variation in detector sensitivity or in image irradiance in the vertical direction over the distance ΔS.

It should be emphasized that detector scanning does not eliminate errors that are due to variations in the sensitivity of the detector with direction of incidence of incident flux. However, the design of the ellipsoidal mirror reflectometer is such that the reflected flux is incident on the detector over a relatively small solid angle, in which the marginal rays strike the detector at an angle of approximately 24° to the normal. Tests [3] have shown that the detector used with this instrument is essentially free from variations in response with angle of incidence at angles of incidence less than 30° to the normal.

A true raster pattern, as shown in figure 8, is difficult to reproduce mechanically. Ideally the detector should scan slowly from

left to right across the image, then fly quickly back to the starting position and down a distance ΔS, in as short a time as possible. An alternative, and equally valid, approach is to scan slowly in both directions, with the detector moving down a distance ΔS at the end of each traverse.

The scanning device that was constructed is shown schematically in figure 9. The detector was mounted on an indexing head, which could be moved in two orthogonal directions x and y by turning two micrometer screws. The screw that controlled the motion in the y direction was driven by a constant speed motor, whose speed could be accurately controlled. The screw that controlled the motion in the x direction was driven by a reversible stepping motor, which reversed direction automatically after a preset number of steps, whose size could also be controlled. The scan pattern produced by the combined motion is thus a steady back-and-forth motion in the x direction superimposed on a slow motion in the y direction which produced two slightly distorted raster patterns, one on top of the other. The two patterns are sketched separately in figure 9. The distortion of the pattern does not invalidate the mathematical analysis.

The equipment used to collect and process the signal from the detector during a scan is shown schematically in figure 10. The signal from the detector produced by the chopped incident flux was synchronously amplified and fed to the electronic integrator, which produced a d.c.

potential proportional to the total energy received by the detector (flux × time). The integrator was controlled by the timer switch in the scanner control, so that both the integrator and scanner were started and stopped simultaneously. The d.c. signal from the integrator was fed to a digital voltmeter.

Tests were made to evaluate the contributions made to the overall uncertainty of measurement by each component. Figure 11 shows schematically the arrangement used to check the integrator. A constant-voltage Zener diode source was used as input to the integrator. An electronic timer, which measured the elapsed time to 0.001 minute, was connected in parallel to the integrator. The integrator was turned on for eight different periods of approximately five minutes each. The signal from the integrator for each period, as read on the digital voltmeter, was divided by the corresponding elapsed time in minutes to obtain the ratios shown in the figure. The standard deviation of the eight measured ratios was 0.015% of the mean value.

Figure 12 shows the arrangement used to test the amplifier and integrator in combination. While the detector was in the circuit, but not irradiated, the "calibrate" signal in the amplifier was used as the input signal. The signal was turned on for 12 periods of approximately one minute each, and the total signal for each period was divided by the elapsed time in minutes to obtain the ratios shown in the figure. The 12 periods were divided into four groups of three each, separated by

6-minute intervals. The overall standard deviation of the 12 values was 0.075% of the mean, and no trend indicating drift could be detected over the period of approximately 1/2 hour required to complete the measurements.

Figure 13 shows the arrangement used to check the scanner and integrator in combination. The input signal was a constant potential from a Zener diode source. The integrator was controlled by the scan control of the scanner, so that the integrator and scanner started and stopped simultaneously. Each scan required approximately 7 minutes, and the scans were recorded in three groups of five, separated by one hour intervals. The overall standard deviation of the 15 scans was 0.057% of the mean, and no trend with time was detected. Actually, what was evaluated in this test was the variation in time of scanning for the 15 scans.

Figure 14 shows the arrangement used to test the Globar source, detector, amplifier and integrator in combination. Again the electronic timer was connected in parallel with the power supply to the integrator. The signal produced by the detector viewing the chopped flux from the Globar was integrated for 13 periods of approximately one minute each, and the integrated signal displayed on the digital voltmeter for each period was divided by the time in minutes for that period, to produce the ratios shown in the figure. One hundred minutes later two additional one-minute ratios were taken. The standard deviation of the first 13 ratios was 0.26% of the mean value, and the mean of the two ratios

obtained 100 minutes later was lower by 0.59%. These results indicate that the major source of uncertainty is in the source-detector combination, and that significant drift with time occurred. The sum of the three other contributions was only 0.095% when summed in quadrature, and 0.147% when summed directly. The test did not reveal whether the uncertainty was due primarily to changes with time in the radiance of the source or in the sensitivity of the detector. However, it is believed that it is due to changes in the radiance of the source.

Figure 15 shows the results obtained with the entire assembly shown in figure 10, when scanning over images that varied in area by a factor of about 4, but which contained the same total flux. The measurements were made in a converging beam, focused by a spherical mirror. Image 2 was obtained with the detector in the focal plane, and image 1 was obtained with the detector at some distance from the focal plane. The relative size of the detector is indicated by the area 3 on the figure. The results in the figure show that the difference in the two mean values, of 0.80% of the mean value, is not statistically significant at the 95 percent level. This is due in part to the relatively high standard deviations of the two means, 0.43 and 0.34 percent respectively. Again the major source of instability is believed to be the Globar source.

The results to date indicate that the mechanical scanner, when used with the ellipsoidal mirror reflectometer, shows promise of yielding reflectance data accurate to perhaps 2%, out to wavelengths considerably

beyond the 7 μm limit reached with the sulfur coated averaging sphere. Time and funds available did not permit the extensive testing which would be required to establish the accuracy and wavelength limits of the instrument when used with a scanning detector.

The radiometric efficiency of detector scanning can be defined as the ratio of the integrated signal from the detector during a scan to the total energy in the image during the time period of a scan. This is a function of the relative sizes of the image to be scanned and the detector. It will be assumed that the smallest (most efficient) scan pattern will be used in each case. Assume that a rectangular detector, of width a and height b, is uniform in response over its entire area, and that a rectangular image of width c and height d is uniform in irradiance over its area. Assume further that both b and d are integral multiples of ΔS, the raster spacing in the scan pattern. The signal from the detector will be proportional to the fraction of its area that is filled by the image.

The equivalent time during a sweep when (1)the image is on the detector, when $a > c$, will be proportional to c, and the signal from the detector (neglecting the effect of the height of the image) will be proportional to a/c; and (2) when the image completely fills the detector, when $c > a$, will be proportional to c, and the signal from the detector during this time (again neglecting the effect of height) will be proportional to one.

The equivalent number of sweeps when (1) the entire height of the image is on the detector, for the case where $b > d$, will be d, and the signal from the detector will be proportional to b/d (neglecting the effect of the width of the image); and (2) the entire height of the detector is filled with the image, for the case where $b < d$, will be b, and the signal from the detector

(again neglecting the effect of the width of the image) will be proportional to one. The total energy in the image during a complete scan will be proportional to the time period of the scan. Thus the general equation for the radiometric efficiency, E, of detector scanning can be expressed as

$$E = \frac{p\,q}{(a+c)\,(b+d)}$$

where p is the smaller of a and c, and q is the smaller of b and d. The maximum efficiency will be 0.25, and will be attained when the detector is the same size as the image. This is a significant improvement over that attained with the sulfur-coated averaging sphere. In essence, if the detector and image are similar in shape and orientation, the efficiency is the area of the detector or image, whichever is smaller, divided by the area scanned.

2.2.2 Inverse Mode Operation

2.2.2.1 Theory of Operation

The ellipsoidal mirror reflectometer is normally operated with the detector at the second focal point of the mirror, and the specimen at the first focal point is irradiated by a beam of small solid angle incident through a hole in the mirror. It is equally valid to locate the source at the second focal point, and collect for measurement the flux reflected by the specimen into a small solid angle through the hole in the mirror. Operation of the reflectometer in this manner is called inverse mode operation.

The principal disadvantage of inverse mode operation is that the specimen may be heated by the incident flux, since such flux includes all wavelengths emitted by the source, and not just a narrow wavelength band,

as is the case in normal operation. The change in flux emitted by the specimen as it warms up could cause an error in the reflectance measurement, particularly if the incident flux is not chopped, as would be the case if an interferometer spectrometer was used as the detector.

The major advantage of inverse mode operation is that the specimen is irradiated uniformly over its entire area and from all angles throughout the hemisphere, provided four conditions are met. These are : (1) that the source be uniform in radiance over its entire area, (2) that the source be uniform in radiance with direction for all angles within about 30° of the normal to its surface, (3) that the source be of such size that all of the image of the specimen, projected to the second focal plane, be contained within the overall area of the source, and (4) that the ellipsoidal mirror be uniform in reflectance over its entire area. These conditions are not difficult to meet.

If the mirror had a reflectance of 1.0 over its entire surface, the irradiance on the specimen would be the radiance of the source times the projected solid angle[1/] subtended by the mirror from the specimen, regardless of the varying magnification factor with position on the mirror. This is true because, in a lossless optical system, the radiance is invariant along any ray, provided the index of refraction of the transmitting medium does not change. In this case air is the transmitting

---

[1/] The projected solid angle is defined as $\int_\theta \int_\psi \cos\theta d\theta d\psi$, where the limits of integration of θ and ψ define the solid angle.

medium. In the real case, the radiance of a particular ray incident on the specimen is the radiance of that ray leaving the source times the transmittance of the optical path. If the reflectometer is in a controlled atmosphere of a non-absorbing gas, the transmittance of the optical path is equal to the reflectance of the mirror.

This property of constant radiance regardless of magnification factor not only corrects for the changes in magnification factor that are inherent in a perfect ellipsoidal mirror, but also for the deviations of the real mirror from a perfect ellipsoid. The only restriction is that any ray leaving the specimen and incident on the mirror must be reflected back to the source. Then if every ray leaving the source and striking the mirror has the same radiance, and the reflectance of the mirror is identical for all such rays, each point on the specimen will be irradiated uniformly over the entire solid angle subtended by the mirror, and the irradiance will be uniform over the area of the specimen.

The uniform irradiance of the specimen obviates the need for any flux averaging. The detector now views the specimen directionally, and will be uniformly irradiated, regardless of the geometrical distribution of flux reflected by the specimen. The flux reflected by a specimen can be compared to that reflected by a good mirror without error due to variations in sensitivity over the area of the detector, and since a beam of small solid angle is incident on the detector in a near normal direction, variations in sensitivity with angle of incidence also have no effect.

When a good mirror, of known reflectance, is used as the comparison standard, the flux ratio measured with the emr in the inverse mode,

divided by the reflectance of the standard, is the hemispherical-directional reflectance factor, neglecting flux losses. The hemispherical-directional reflectance factor is defined as the ratio of the flux reflected by a specimen, that is uniformly irradiated over a hemisphere, into a small solid angle about a specified direction, to that reflected by an identically irradiated specimen of the ideal completely reflecting, perfectly diffusing surface into the same small solid angle.

If the mirror comparison standard is oriented so that none of the optical path from the source to the detector is blocked, the radiance of any ray reaching the detector will be the radiance of that ray as it leaves the ellipsoidal mirror times the reflectance of the standard (if there is no atmospheric absorption). The irradiance on the detector will be the radiance mentioned above times the cosine of the angle of incidence on the detector times the solid angle of view of the detector (the specimen or standard always overfills the solid angle of view). This irradiance, when corrected for the known reflectance of the comparison standard, is the same as the irradiance that would be produced by a specimen of the ideal completely reflecting perfectly diffusing surface, when irradiated over a complete hemisphere with the same incident radiance. (See Appendix A.) In the real case, however, the specimen is not irradiated over a complete hemisphere. The ellipsoidal mirror does not reflect over the area of the hole, and part of the beam from the source is blocked by the specimen and its support. Corrections must be made for these known flux losses, and they can be made simply for the ideal standard from the

geometry of the system. The ratio of the detector output when a sample is measured, to that when the mirror standard is measured, corrected for the known reflectance of the standard and the known flux losses, is the true near-hemispherical-directional reflectance factor of the specimen, where the term "near-hemispherical" refers to the actual geometry of the system used, which approximates hemispherical irradiation and directional viewing.

The true hemispherical-directional reflectance factor of any specimen is, by the Helmholtz reciprocity theorem, equal to the directional-hemispherical reflectance factor (if the geometry is identical for the two cases, only the direction of propagation of the radiant energy being reversed), which is in turn equal to the directional-hemispherical reflectance.

The measured near-hemispherical-directional reflectance factor of specimens that are good diffuse reflectors, corrected for the reflectance of the standard and the lost incident flux, will be a very close approximation to the true hemispherical-directional reflectance factor, and need not be corrected for actual losses in reflected flux. Samples that are good specular reflectors can be oriented to avoid flux losses, and no corrections are needed. In this case the specular sample is compared directly to the mirror standard of known reflectance. For specimens that depart significantly from perfectly diffuse or specular reflectance, it is necessary to correct for the contribution to the reflected flux that would be made by the lost incident flux. This can be done by the techniques used with the emr when used in the direct mode, as described in reference [3].

2.2.2.2 Experimental Results

Because of the deobligation of funds it was not possible to establish the accuracy and precision of the ellipsoidal mirror reflectometer when used in the inverse mode. However, satisfactory operation was attained at 8.4 and 14.0 μm. A circular source, 10 cm in diameter, was located in the second focal plane, with a chopper immediately above it. The source was maintained at about 100°C. A mirror was used as the specimen, and was tilted so that the angle between the major axis of the ellipse and the beam incident on the specimen was varied from 12° to 84°, and from -12° to -84°, in order to check the uniformity of the source radiance and the ellipsoidal mirror reflectance.

The readings varied with position by as much as ±2.5%, and could be repeated to about 0.1%. These results suggest strongly that the instrument is usable to 30 μm or beyond, and that the overall error in the measured reflectance, without correction, should not exceed about 2.5% for diffusely reflecting specimens or 0.5% for specularly reflecting specimens. The precision of measurement should be better than 0.5%. Residual errors in reflectance measurements corrected by the techniques described in reference 4 should not exceed 1% for any specimen.

It should be emphasized that the above tentative conclusions are based on inadequate data, but they are believed to be realistic.

3. The Interferometer Spectrometer

3.1 Background and Theory

The following discussion is based in part on the Block Engineering

service manual supplied with the interferometer spectrometer, and on reference 12. Reference 13 gives an extensive bibliography on spectroscopy in general, including many references on Fourier spectroscopy.

The Michelson interferometer consists of two plane mirrors mounted at right angles to each other, with a beamsplitter (a partially [50%] transmitting mirror) bisecting the angle between the mirrors. An entrance aperture is located opposite one mirror, and an exit aperture opposite the other. One of the mirrors can be moved back and forth in a direction normal to its surface. A cross-sectional drawing of such an interferometer is shown in figure 16.

For purposes of discussion, assume that the beamsplitter S (figure 16) reflects half and transmits half of the radiant energy incident upon it, and that the mirrors are perfect reflectors. A beam of radiant energy entering through the entrance aperture e_1 will be divided into two equal portions, A and B, by the beamsplitter. The A portion, transmitted to the movable mirror M_1, will be reflected back along its original path to the beamsplitter, where it is again divided into two equal portions, A_1 transmitted and passing back out the entrance aperture, and A_2 reflected to the exit aperture, e_2. The B portion of the incident beam is reflected by the beamsplitter to the fixed mirror M_2, and reflected back to the beamsplitter, where it is again divided into two equal portions, B_1 reflected back out the entrance aperture e_1, and B_2 transmitted to the exit aperture, e_2. Thus, two equal beams, A_2 and B_2, each comprising one-fourth of the incident beam, will be transmitted through

the exit aperture, e_2, toward the detector.

If the incident beam is monochromatic, an interference pattern will be formed by the two beams A_2 and B_2 passing out the exit aperture. This pattern will consist of a light or dark circular area at the center, surrounded by circular fringes, alternately light and dark. The width of the fringes, and hence the diameter of the circular area at the center, is a function of (1) the difference in path length of the two beams, (2) the dimensions of the interferometer, and (3) the degree of collimation of the incident beam. The difference in path length may be measured in units of wavelength, λ, of the incident beam, and should include the effects of phase changes on reflection at the mirrors and on reflection and refraction at the beamsplitter. If the incident monochromatic beam is perfectly collimated, which can only be approached in practice, or if the optical path lengths for the two beams are identical, the central area will occupy the entire field, and there will be no fringe pattern. When the path lengths are equal, the image of mirror M_2 reflected in the beamsplitter will exactly coincide with mirror M_1. As mirror M_1 is moved away from this position in a direction normal to its surface, circular fringes will appear at the outer edges of the field and will move radially toward the center, and the number of fringes in the pattern will increase. As the mirror is moved through the distance $\lambda/2$, the difference in path length for the two beams increases by one wavelength, λ, and each fringe will go through a complete cycle from bright to dark to bright. The

effect of this cyclic change is to cause the dark fringes to appear to move radially from the center to the edge of the field, while the whole pattern moves inward. In effect, for each distance $\lambda/2$ that mirror M_1 moves, a new fringe originates at the center of the pattern and as the mirror movement continues, the dark fringe moves radially outward, but never disappears from the field. As more fringes appear, the width of each fringe decreases, and the diameter of the first distinct ring at the center becomes smaller.

In a properly designed optical system the dimensions of the system, the distance over which mirror M_1 moves and the degree of collimation of the incident beam are all controlled so that only the central portion of the area inside the first distinct ring reaches the detector. Under these conditions there will be complete destructive interference, and no signal from the detector, whenever the difference in path lengths is $\lambda/2$ or an odd multiple of $\lambda/2$ ($\pm\lambda/2$, $\pm3\lambda/2$, $\pm5\lambda/2$, etc.) and complete constructive interference, and a maximum signal from the detector, whenever the difference in path length is zero or an integral multiple of λ ($\pm\lambda$, $\pm2\lambda$, $\pm3\lambda$, etc.).

When the path lengths are identical, the radiance, L, at the center of the pattern will be equal to L_o, the radiance on the entrance port of the interferometer, and as mirror M_1 is moved away from the image of M_2, the radiance at the center of the fringe pattern will vary sinusoidally [5] as the difference in path lengths increases, according to the equation

$$L = 0.5\ L_o\ (1 + \cos 2\pi\ \nu\ B\ t/T) \qquad (22)$$

where ν is the wavenumber of the incident flux in cm^{-1} ($\nu = 1/\lambda$), B/2 is the displacement of the movable mirror in the time interval T, or sweep time, and t is the time elapsed from the beginning of a sweep (see figure 17). Bt/2T is the displacement of the mirror, x, at time t. Equation (22) shows that the frequency of the signal from the detector is related to the wavenumber ν of the incident flux and the mirror velocity, B/2T. Since the difference in path length is twice the mirror displacement, we can write

$$F_\nu = 2 \cdot \nu \cdot B/2T = \nu B/T \qquad (23)$$

where F_ν is the frequency of the signal from the detector. Thus for flux of any given wavelength, the frequency F_ν of the signal from the detector is directly related to mirror velocity.

Equations (22) and (23) can also be derived by considering the doppler shift of the frequency of the flux incident on the moving mirror M_1, which will then beat with the flux from the stationary mirror, M_2, when the two beams are combined. The two explanations are completely compatible, and lead to the same results.

The above explanation is simplified since perfect mirrors and perfect beamsplitters do not exist, and polarization effects cannot be neglected. However, the explanation is qualitatively correct, and

equation (23) is rigorously correct. With real materials it is generally not possible to make the two beams reaching the detector exactly equal, and there is always some absorption at the mirrors and beamsplitter. If the two beams are not equal, there will be a uniform radiance, equal to the difference in radiance of the two beams, superimposed on the fringe pattern. Since the signal from the detector is amplified by an a.c. amplifier, the signal from the uniform radiance is not amplified, and is lost. There is an instrument calibration factor, η, that must be inserted into equation (22) to account for losses and the failure of the beamsplitter to split the incident beam into two equal portions.

$$L = \eta\ 0.5\ L_o\ (1 + \cos 2\pi\ \nu\ Bt/T) \qquad (24)$$

The instrument calibration factor, η, is wavelength dependent, and includes polarization effects as well as those effects mentioned above.

When polychromatic flux is incident on the interferometer entrance port, the detector output is not a single audio-frequency sine wave, but is made up of superimposed audio frequencies corresponding to the optical frequencies of the incident flux. If an ideal interferometer was used, the amplitude of each audio frequency, F_ν, would be directly proportional to the spectral radiance, L_λ, of the incident flux at the corresponding wavenumber, ν, as indicated in equation (22). However, for a real interferometer, if values of L_o are desired, η must be evaluated for the interferometer over the entire wavelength range of interest. If the instrument is to be used only for evaluating flux ratios it is not necessary to calibrate the equipment for η_λ, since it appears in both numerator

and denominator.

The output of the detector for a scan, plotted as a function of time (or distance of travel of the movable mirror) is known as an interferogram [12], and is the Fourier cosine transform of the radiant spectrum of the beam entering the spectrometer. Interferograms can be added and subtracted without reduction, but not multiplied or divided. When the incident beam is monochromatic, the interferogram is a sine wave whose amplitude is proportional to the radiance of the beam, and whose period is proportional to the wavenumber (frequency) of the radiant energy in the beam. When the incident flux is heterochromatic, all of the sine waves representing the different wavenumbers in the incident beam will be in phase when the optical path lengths of the two beams are identical, and more and more out of phase as the path length difference increases. Figure 18 is a typical interferogram for a heterochromatic source. It is difficult to predict from the shape of the interferogram the shape of the spectral distribution curve of the polychromatic incident flux, but the height of the center peak is an indication of the total flux in the beam.

The wavelength, or wavenumber, resolution of a spectrometer is a measure of its ability to separate or resolve two adjacent peaks. It can be specified as the smallest increment of wavelength (or wavenumber) that can be distinguished in the spectral curve. The theoretical resolution limit of an interferometer spectrometer, $\Delta\nu$, is given by

$$\Delta\nu = K/B \qquad (25)$$

where K is determined by the refraction at the entrance aperture, and B is the maximum internal retardation. For the Block interferometer, K = 1, approximately. The theoretical limit is never attained in practice.

The spectral distribution of flux in the incident beam can be obtained from an interferogram in two ways. In the first method, referred to as analog reduction, the interferogram is recorded on an endless magnetic tape and played back into a narrow-band variable frequency bandpass filter, which is slowly tuned over the appropriate audio frequency range. The amplitude recorded at each audio frequency is then a measure of the spectral radiance of the incident beam at the corresponding wavenumber. A less convenient, but more accurate method, referred to as digital reduction, is to record the interferogram in digital form, enter it into an electronic digital computer, and compute the inverse Fourier transform.

3.2 Description of Block Interferometer

A Block Engineering Model 200 interferometer spectrometer was purchased for use on this project. The instrument was equipped with an interferometer head designed to cover the wavelength range of 250 to 2500 cm^{-1} (40 to 4 μm). The optical head and detector mount are each about 3.5 by 3.5 by 7.5 inches in size, and can be separated. A hot-filament source, in a mount of similar size, was also provided. The

source can be attached to the optical head (interferometer) to provide a "chopped" beam of flux.

The movable mirror, M_1, is attached to the armature of an electromagnet, and is displaced by changing the direct current through the solenoid. Figure 19 is a block diagram of the electronic system used with the interferometer. The mirror drive transducer is located on the optical head, and the bias network and preamplifier are located on the detector mount. A single power supply and voltage regulator is used for the amplifier, sweep generator and drive amplifier. The sweep generator forms a saw-tooth wave of the form shown in figure 17, which is amplified by the drive amplifier. The sweep period, which is T+F+R (figure 17) can be preset to 0.25, 0.50 or 1.0 sec, and the bias voltage, which corresponds to the minimum voltage of the wave, can also be adjusted to vary the position of the mirror at the beginning of a sweep. For best results in analog and some forms of digital reduction of the interferograms, it is important that the center of the sweep be located accurately at the positions where the path lengths for the two beams are equal.

The data output of the amplifier is recorded in a computer memory, called a co-adder, mounted in the control cabinet. The interferogram is sampled at a number of points, equally spaced in time, and the signal is converted from analog to digital and stored in the computer memory. The sampling timer is started by a trigger pulse at the beginning of a sweep, which is always generated at the same position of the movable mirror. The data points correspond to the signal from the detector at equally

spaced positions of the movable mirror. The data for each point is stored in a specific memory bank, and points for the corresponding times in successive scans will be stored in the same memory bank. Thus the co-adder can be used to coherently add the data for a number of successive scans. This feature can be used to greatly increase the useful signal-to-noise ratio, because the signal increases directly with the number of scans, and the noise, being random, increases as the square root of the number of scans. The instruction manual accompanying the Block instrument indicated that the data were recorded at 1024 points during a 1-second sweep. However, the instrument that was delivered recorded only 521 points, which indicates that a change had been made after the manual was written.

The data from the co-adder memory could be read out through a digital-to-analog converter and recorded on an endless belt of magnetic tape, in the wave analyzer used for analog reduction of the data. The co-adder was also designed so that the data could be read out in digital form for direct entry into an electronic digital computer, or for storage in digital form on magnetic or punched paper tape.

3.3 Interface Problems

The interferometer spectrometer, as received from the manufacturer, operated satisfactorily for analog reduction of the data, but it was not possible to read out the data in digital form. A TWX coupler was used to control the readout of the data in digital form, which was then fed either directly to a computer by use of an acoustic coupler and

data-phone hookup, or to a teletype machine for recording in typed form and on punched paper tape. Interface problems were present, apparently due to noise in the TWX coupler, which reacted with the control circuit of the co-adder, and caused erratic operation, and at times even wiped out data from some memory banks.

The TWX coupler and co-adder were returned to the manufacturer's representative for solution of the problem. When the instrument was returned, the problem of reaction of the TWX coupler with the control circuits had been solved, but transients generated when the TWX coupler or Teletype machine were turned on still wiped out the data from the first few memory banks of the co-adder memory. The problem was finally eliminated by connecting the cases of the teletype, TWX coupler and co-adder to a common ground. Apparently the trouble was associated with ground loop problems or a floating ground.

3.4 Computer Code for Data Reduction

It was necessary to develop a computer code to obtain the Fourier cosine transform of the interferogram as recorded.

The digital data are stored in the co-adder memory as 521 16-bit binary words. Each word consists of a sign bit followed by 15 binary bits. The maximum capacity of any one memory bank is thus ±32,767 in decimal notation, and the maximum difference between any two words is 65,534.

The TWX coupler reads out the data from the co-adder memory one bit at a time, and converts each 16-bit binary word into a 6-digit octal

word in ASCII code, which is then recorded by a Teletype machine on punched paper tape and typed out simultaneously. Negative words are recorded as 8's complement. The first bit of the binary word is a sign bit. The plus sign is recorded directly, but the minus sign is recorded as a slash, /, to distinguish the 8's complement negative numbers from true negative numbers. The next 15 bits are read in groups of three, and converted to an octal digit. When the entire interferogram is completely recorded the record consists of 521 octal numbers, some positive and some negative, in ASCII code.

The first step in the data reduction is to transfer the data from punched paper tape to magnetic tape for entry into the computer. This is done on a Digi-data converter, and produces a magnetic tape suitable for entry into the 1108 computer.

On the computer a sub-routine CHAR picks up the characters from the magnetic tape and stores them in the computer memory. Only 512 of the 521 words are used. The first three words are discarded, because they may have spuriously high values, which distort the spectrum. The last six words are also discarded.

The computer first converts the negative numbers from 8's complement to true negative octal numbers by subtracting them from 77778, then converts all numbers from octal back to binary.

The subroutine FSER computes the Fourier coefficients A_k, B_k of the Fourier series

$$YE(x) = \frac{Ao}{2} \sum_{K=1}^{256} (A_k \cos Kx + B_k \sin Kx) \qquad (26)$$

where YE(x) is the amplitude of the interferogram at time or position x. The YE values are the recorded words, and the x values are the serial numbers, from 1 to 512, of the recorded words.

Next, monochromatic flux values Φ_k at wavenumbers (or wavelengths) corresponding to the points K(K = 1 to 256) are computed as

$$\Phi_k = \sqrt{A_k^2 + B_k^2} \qquad (27)$$

The A_k, B_k values are then used as input, and the inverse Fourier transform is computed to give YE_c values. A Calcomp plotter is used to plot the original YE values as a function of x, and then the YE_c values are plotted on top of this curve. Any difference in the two curves indicates an error in the computations.

The Φ_k values are plotted as a function of K to give the output of the interferometer spectrometer in terms of a spectral distribution. However, this is not the true spectral flux density of the beam incident on the entrance aperture of the interferometer, because there is an instrument calibration factor η_k for each K value, as indicated in equation (24), and these η_k calibration factors vary widely with the value of K. No attempt was made to evaluate the η_k values, since we are interested primarily in use of the interferometer spectrometer in reflectance measurements, where ratios of fluxes are involved. The

η_k values factor out when ratios are taken, hence do not affect the results.

3.5 Tests of Interferometer Spectrometer

Tests were made to evaluate the operating characteristics of the interferometer spectrometer.

3.5.1 Wavelength Calibration

The first test was to establish the wavelength, or wavenumber, calibration of the instrument. Two methods were used. The instrument was set up to view the beam produced by a prism monochromator, with the wavelength drive set to give wavelengths in the range of 4 to 15 microns. Next, the instrument was set up to view a Globar source, and the signal was recorded for 300 scans. A polystyrene film was then placed over the entrance aperture to the interferometer, and the signal was subtracted for 300 scans from that previously recorded. The resulting interferogram, when reduced, gave a negative absorption curve for the polystyrene film.

The calibration curves were digitally reduced, and the known wavenumbers were plotted as a function of point number. The resulting curve appeared to be a straight line, which nearly intersected the origin. A least-squares curve was computed for the data, and had the equation

$$Y = -22.029 + 10.233\ K \qquad (28)$$

where Y is the wavenumber corresponding to the serial number of point K ($25 < K < 257$). The estimated standard deviation of the slope was computed

to be 0.014, or 0.13%, and that of the intercept was computed to be 2.42. The standard deviation of the experimental points about the computed line was 8.65 wavenumbers. Thus the wavenumber calibration appears to be reproducible to about ±10 wavenumbers, which might also be inferred from the theoretical resolution of the instrument, which is reported by the manufacturer to be 20 wavenumbers.

3.5.2 Angular Sensitivity

Tests were made to determine the variation in response of the detector with angle of incidence of the incident beam. The interferometer was attached to the source, and the optical axis of the system was taken as the normal to the exit window of the interferometer. The detector was positioned in a plane normal to the optical axis and 28 inches from the interferometer. The 28 inches was measured from the case adjacent to the exit window to the front of the detector case. Readings taken at various positions along a horizontal line perpendicular to the optical axis are shown in figure 20, and those along a vertical line perpendicular to the optical axis in figure 21. The results indicate that the position of maximum response is located two inches above and one inch to the right of the optical axis. The long dimension of the source was vertical, which may account for the beam appearing to be wider in the vertical direction than in the horizontal direction.

Similar tests in which the interferometer was attached to the detector gave similar results, which indicates that the apparent spread of the beam is due to the optics of the interferometer,

rather than the detector or source. When the source was positioned so that its image, in the plane of the detector, was horizontal, a more nearly symmetrical pattern was observed, and the maximum response was significantly lower. This suggests that the sensitive area of the detector may be rectangular, with one dimension much longer than the other.

All of the above tests were made using analog reduction of interferograms, and the Block heated filament source. Tests indicated that the temperature of the source fluctuated significantly over a period of a few minutes, so that its radiance might change by as much as 5%. Also the reproducibility of analog reduction on the same interferogram was no better than two or three percent. For these reasons the above results must be considered as only semi-quantitative. They are however, sufficient to show that the interferometer spectrometer field of view is too small to make it suitable for use as a detector located at the second focal point of the ellipsoidal mirror reflectometer.

3.5.3 Strong Reflectometer

Perhaps the simplest and most accurate reflectometer known is the Strong reflectometer [12] for measuring the reflectance of near-perfect mirrors. It was believed that measurements with an instrument of this type, with the interferometer spectrometer employed as the detector, would give a quantitative indication of the degree of accuracy and precision that might be attained with the interferometer spectrometer.

The method is based on measuring the spectral radiance of the source

when reflected once by a reference mirror, then when reflected three times, twice by the test mirror and once by the reference mirror. The ratio of the thrice reflected radiance to the once reflected radiance is then the square of the reflectance of the test mirror.

In order to reduce errors due to fluctuations in the radiant output of the source, a constant radiance Globar source was used. The radiance of the Globar was monitored by a solar cell, whose output was used in a feedback circuit to control the voltage to the Globar and keep its radiance constant. As further precautions, the power to the Globar control was supplied through a voltage regulator, which maintained the input potential constant to 0.01%, and the Globar was mounted in a water-cooled housing, through which water from a constant-temperature (55°F) heat exchanger was circulated. No fluctuation of the source radiance was detected over periods of up to 30 minutes.

Figure 22 is a sketch of the optical path in the reflectometer. The Globar source housing had a rectangular aperture, 3/16 wide and 1/4 in. high, directly in front of the Globar. An image of the source was focused by means of a 28-in. radius spherical mirror onto the first reference aluminum mirror, 1/4 in. wide by 3/4 in. high. A second 28 in. radius spherical mirror focused the image from the reference aluminum mirror onto the aperture in an aperture plate, which was viewed by the interferometer spectrometer from a distance of 4 in. The field stop of this system was 1/4 in. high and 1/8 in. wide, and was formed by the image of the aperture in front of the Globar, 3/16 in.

wide by 1/4 in. high, superimposed on the aperture in the aperture plate in front of the interferometer spectrometer, which was 1/8 in. wide by 3/4 in. high. The limiting aperture stop was a 3 in. diameter hole in a mask in front of the first spherical mirror.

The test mirror was mounted in a slide that moved in a slot parallel to the surface of the first reference aluminum mirror. The second aluminum reference mirror, identical to the first, was mounted parallel to and facing the first reference mirror, positioned so that both were normal to and centered about a single line normal to their surfaces, and equally distant from the plane of the front surface of the test mirror.

In essence a reflectance measurement consisted of recording two interferograms, one with the test mirror out of the optical path so that the beam from the source to the detector was reflected once from the first reference mirror, and the second with the test mirror in the optical path, so that the beam from the source to the detector was reflected twice by the test mirror and once by the second reference mirror. The two interferograms were reduced, and the spectral reflectance of the test mirror was taken as the square root of the ratio of the spectral flux reflected twice by the test mirror and once by reference mirror 2 to that reflected once by reference mirror 1. Both beams were reflected once each by the two spherical mirrors and the plane mirror in front of the aperture plate, hence the effect of these reflections cancelled out in taking the ratio.

There were several factors that introduced errors into the measurement that were corrected for. The interferometer spectrometer field of view was appreciably larger than the small hole in the aperture plate. The detector usually operated at a temperature above ambient. As a result, the background, measured with the source blocked off, was negative. The net flow of radiant energy was from the warm detector to the cooler surroundings. When the source was blocked and the background subtracted, the height of the spectral flux distribution curve was increased by as much as 25% at the long wavelengths (low wavenumbers), while the height at short wavelengths was not appreciably affected. The effect of not subtracting background was to give low values of reflectance at the long wavelengths. For instance, when the background increased the signal by 25%, a reflectance, measured without background correction, of 0.985 was changed to 0.988 when the background was subtracted, and a reflectance of 0.970 to 0.976. Figure 23 is a typical analog record, with and without background subtraction.

A shutter of 1/2-in. aluminum plate was constructed and mounted so that it could be inserted into the optical path a few inches in front of the source. Tests showed that heating the shutter to a temperature 10°C above ambient did not detectably affect the background reading. Hence it was considered unnecessary to cool the shutter. When using about the highest gain setting that did not overload the amplifier, 300 scans nearly filled the co-adder memory. This number of scans was therefore chosen for use in recording data. It required 5 minutes to record

300 scans of the maximum sweep length, and this time was considered not unreasonable, particularly since about 7 minutes was required to record one interferogram on punched paper tape. The signal-to-noise ratio for 300 scans should be about 17 times that for one scan. The procedure finally adopted as standard was to subtract (from zero) the background for 150 scans, with the shutter blocking the beam near the source, then open the shutter and record the signal for 300 scans, and finally close the shutter and subtract background for 150 scans. The background signal showed some drift, particularly as room temperature or the detector temperature changed with time. By subtracting background both before and after the desired signal, the effects of drift were largely compensated for.

The second factor tending to affect the measurements was atmospheric absorption. The atmospheric absorption changed significantly with time, even during a single run. Atmospheric absorption in the 4 to 40 μm range is due almost entirely to carbon dioxide and water vapor. Both of these gases are major constituents of human breath, and their control is difficult without enclosing the volume to be controlled. If the absorption remains constant during the period of a measurement, it will not affect the accuracy, but it will reduce the intensity of the beam reaching the detector, and hence will reduce the sensitivity of the measurement, and increase the statistical error in the wavelength bands where absorption occurs. The entire specular reflectometer, including the interferometer spectrometer and source, was enclosed in a plastic shield, and water-free

CO_2-free air, which had been passed through an air purification system, was fed into the enclosure at a rate of about 85 liters per minute. The air purification system has been previously described [2]. It consisted of an oil-free compressor, a catalytic air dryer, various air filters, two CO_2 absorbing towers filled with Askarite, a silica gel drying tower, a water molecular sieve, plus the necessary pressure reducers, valves and a flow meter. The dew point of the air delivered to the enclosure was below -100°C, and the air was essentially free from CO_2. Figure 24 shows typical spectra produced by analog reduction of interferograms of a Globar source. The top curve was recorded in the purified atmosphere, and the middle curve in ambient atmosphere. The bottom curve is the difference between the two top curves, and represents the observed absorption in the ambient atmosphere. This is shown more clearly in figure 25, which was obtained by digital reduction of similar interferograms. The curve in figure 25 is a spectral plot of the amplitude of the curve obtained in the purified atmosphere minus that of the curve obtained in the ambient atmosphere, divided by the amplitude of the curve in the purified atmosphere. It represents the absorptance of the ambient atmosphere for a path length of approximately 10 feet, if the purified atmosphere is considered to be completely non-absorbing, which has not been proved conclusively.

The third error in the reflectance measurements resulted from differences in the spectral reflectance of the two small aluminum reference mirrors. The square root of the ratio of the reflectance of

the two mirrors was measured, and was found to vary somewhat with wavelength in the range of 1.003 to 0.992, but the overall average ratio was 0.9980. The measured values were corrected for the observed difference in reflectance of the two aluminum reference mirrors.

4. Summary

An improved version of the ellipsoidal mirror reflectometer was designed, and construction was nearly completed. The new design provides for measurements to be made in a controlled atmosphere and increases ease of operation. Tests indicated that use of a detector-scanner combined with an electronic integrator would permit measurements to be made at wavelengths out to 15 μm or beyond with an overall error that should not exceed about two percent of the measured value. Operation of the ellipsoidal mirror reflectometer in the inverse mode showed definite promise of increasing the usable wavelength range substantially without loss in accuracy, but deobligation of funds curtailed the work before accurate evaluations of the usable wavelength range and overall accuracy could be completed. Use of an interferometer spectrometer with the ellipsoidal mirror in the inverse mode appears entirely feasible, but time did not permit such operation to be investigated.

An interferometer spectrometer was used to measure reflectance of high-quality mirrors over the wavelength range of approximately 4 to 30 μm, to an accuracy of better than one percent of the measured value. A computer code was developed for reduction of interferograms.

USCOMM-NBS-DC

References

1. Richmond, J. C. Some Methods Used at the National Bureau of Standards for Measuring Thermal Emittance at High Temperatures, in Surface Effects on Spacecraft Materials, F. J. Clauss, Ed. p. 191 - J. Wiley & Sons, Inc. (1960).

2. Richmond, J. C., DeWitt, D. P., and Hayes, W. D., Jr. Procedures for Precise Determination of Thermal Radiation Properties, November 1962 to October 1963. NBS Technical Note 252 (Nov. 20, 1964).

3. Richmond, J. C., Dunn, S. T., DeWitt, D. P. and Hayes, W. D., Jr. Procedures for Precise Determination of Thermal Radiation Properties, November 1963 to October 1965. NBS Technical Note 267 (Dec. 17, 1965).

4. Dunn. S. T., Richmond, J. C. and Wiebelt, J. A. Ellipsoidal Mirror Reflectometer. J. Res. NBS, Part C, Engineering and Instrumentation 70C [2] 75-88 (April-June 1966).

5. Dunn, S. T., Geist, J. C., Moore, D. G., Clark, H. E. and Richmond, J.C. Thermal Radiation Property Measurement Techniques. NBS Tech. Note 415 (April 1967).

6. Richmond, J. C. Relation of Emittance to Other Optical Properties. J. Res. NBS, Part C, Engineering and Instrumentation 67C [3] 217-225 (1963).

7. Strong, J. Concepts in Classical Optics. (W. H. Freeman and Co., San Francisco, 1958) p. 124.

8. Geist, Jon, Kneissl, G. J., and Weidner, V. R. High Purity Powdered CsI as a High Reflectance Infrared Diffuser, Applied Optics 6 1280 (July 1967).

9. Kneissl, G. J. and Richmond, J. C. A Laser-Source Integrating Sphere Reflectometer. NBS Technical Note 439, (February 1968).

10. Blevins, W. R. and Brown, W. J., J. Sci. Instr. 42, 19 (1965).

11. Kneissl, G. J. Design Study of a Fourier Spectrometer Ellipsoidal Mirror Reflectometer System, Final Report, NASA Ames Research Center, Moffet Field, Calif. Contract NAS 2-4232 (1968).

12. Mertz, L., Transformations in Optics, (J. Wiley and Sons, Co., New York, 1965).

13. Kneubühl, Fritz, Diffraction Grating Spectroscopy, Appl. Opt. 8, [3] 505-519 (March 1969).

14. Strong, J., Procedures in Experimental Physics, (Prentice-Hall, Inc., Englewood Cliffs, N.J., 1938) p. 376.

15. Nicodemus, Fred E., Directional Reflectance and Emissivity of an Opaque Surface, Appl. Opt. 4, 76F-773 (1965).

16. Edwards, D. K., Gier, J. T., Nelson, K. E. and Roddick, R. D., Integrating Sphere for Imperfectly Diffuse Samples, J. Opt. Soc. Am. 51, 1279-1288 (1961).

17. Judd, D. B. Terms, Definitions and Symbols in Reflectometry, J. Opt. Soc. Am. 57 [4] 445-452 (April 1967).

Appendix A

Bi-directional reflectance, $\rho(\theta,\psi;\theta',\psi')$ is defined as

$$\rho(\theta,\psi;\theta',\psi') = \frac{L'dA\cos\theta'd\omega'}{L\,dA\cos\theta\,d\omega} \qquad (A1)$$

where L is radiance incident on area dA of a surface from the solid angle $d\omega$ about a direction θ,ψ, and L' is the reflected radiance from area dA into solid angle $d\omega'$ about the direction θ', ψ'. Since dA appears in both numerator and denominator, it cancels out. The bi-directional reflectance is a dimensionless ratio, and hence cannot be integrated. A more useful term is the relative radiance [9] $\ell(\theta,\psi;\theta',\psi')$ which is defined as

$$\ell(\theta,\psi;\theta',\psi') = \frac{L'(\theta',\psi')}{L(\theta,\psi)\cos\theta d\omega} = \frac{\rho(\theta,\psi;\theta',\psi')}{\cos\theta'd\omega'} \quad . \qquad (A2)$$

This quantity is the same as the partial reflectance [15] and reflectance distribution function [16] of previous authors.

In the discussion that follows unprimed symbols will be associated with incident radiant energy, and primed symbols with reflected radiant energy. The flux Φ_o incident on the area ΔA of a specimen in the ellipsoidal mirror reflectometer (emr) when used in the direct mode (see figure 1A), is

$$\Phi_o = L\Delta\omega\Delta A\cos\theta \qquad (A3)$$

where $\Delta\omega$ is the solid angle of the incident beam. The reflected radiance $L'(\theta'\psi')$ in a direction $\theta'\psi'$ is

$$L'(\theta',\psi') = L\Delta\omega\cos\ \theta\ell(\theta,\psi;\theta'\psi') \tag{A4}$$

and the total reflected flux Φ', is

$$\Phi' = \int_{\theta'=0}^{\pi/2} \int_{\psi'=0}^{2\pi} L\Delta\omega\cos\ \theta\ell(\theta,\psi;\theta'\psi')\Delta A\ \cos\ \theta'\ \sin\ \theta' d\theta' d\psi' \tag{A5}$$

and if none of the reflected flux is blocked or lost, it will all be collected by the ellipsoidal mirror and focused onto the detector. The output, O, of the detector is $\Phi'\rho_e R$, where ρ_e is the reflectance of the mirror and R is the responsivity of the detector.

$$O = R\rho_e L\Delta\omega\Delta A\ \cos\theta \int_{\theta'=0}^{\pi/2} \int_{\psi'=0}^{2\pi} \ell(\theta,\psi;\theta'\psi')\cos\ \theta'\ \sin\ \theta' d\theta' d\psi' \tag{A6}$$

When a specular standard of reflectance ρ_s is used, figure 1B, the incident flux will be specularly reflected by the standard, and the flux Φ' is

$$\Phi_s' = \rho_s L\Delta\omega\Delta A''\ \cos\ \theta'' \tag{A7}$$

where θ'' is the angle of incidence on the standard and $\Delta A''$ is the

irradiated area of the standard. The output, O_s, of the detector will be $\Phi'_s \rho_e R$. The measured ratio then is Φ'/Φ'_s.

$$\frac{O}{O_s} = \frac{R\rho_e L\Delta\omega\Delta A \cos\theta \int_{\theta'=0}^{\pi/2}\int_{\psi'=0}^{2\pi} \ell(\theta,\psi;\theta',\psi') \cos\theta' \sin\theta' d\theta' d\psi'}{R\rho_e\rho_s L\Delta\omega\Delta A'' \cos\theta''} \qquad (A8)$$

But the same incident beam is used in both cases, hence $\Delta A \cos\theta = \Delta A'' \cos\theta''$, and

$$\frac{O}{O_s} = \frac{1}{\rho_s} \int_{\theta'=0}^{\pi/2}\int_{\psi'=0}^{2\pi} \ell_\eta(\theta,\psi;\theta',\psi') \cos\theta' \sin\theta' d\theta' d\psi' \qquad (A9)$$

The directional-hemispherical reflectance $\rho(\theta,\psi:2\pi)$ of a surface is the ratio of the flux incident on the surface from a small solid angle $\Delta\omega$ about the direction θ, ψ, that is reflected by the surface into a hemisphere.

$$\rho(\theta,\psi;2\pi) = \frac{L\Delta A \cos\theta\Delta\omega \int_{\theta'=0}^{\pi/2}\int_{\psi'=0}^{2\pi} \ell(\theta,\psi;\theta',\psi') \cos\theta' \sin\theta' d\theta' d\psi'}{L\Delta A \cos\theta\Delta\omega} \qquad (A10)$$

hence when used in the direct mode the emr measures the directional-hemispherical reflectance divided by the reflectance of the mirror

standard, neglecting flux losses.

When the emr is used in the inverse mode, figure 2A, the specimen at the first focal point is irradiated over a hemisphere by a large-area source in the second focal plane centered on the second focal point, and is viewed by a detector through a small hole in the mirror. To preserve the analogy with the emr when used in the direct mode, primed symbols will be used for terms associated with incident radiant energy, and unprimed symbols with reflected radiant energy, in the following equations. The subscript i will be used to denote the inverse mode.

The flux $d\Phi_i'$ incident on area ΔA of the specimen over a small solid angle $d\omega'$ centered about a direction θ', ψ' from the specimen surface is

$$d\Phi_i' = \rho_e \, L_i' \, d\omega' \Delta A \cos \theta' \tag{A11}$$

where L_i' is the radiance of the beam leaving the source. The reflected radiance $dL_i(\theta,\psi)$ of the specimen in the direction of the detector, due to $d\Phi_i'$, is

$$dL_i(\theta,\psi) = L_i' \, d\omega' \cos \theta' \rho_e \ell(\theta'\psi';\theta,\psi) \, . \tag{A12}$$

Since the specimen is irradiated over a hemisphere, the total reflected radiance $L_i(\theta,\psi)$ in the direction of the detector, is

$$L_i(\theta,\psi) = \int_{\theta'=0}^{\pi/2} \int_{\psi'=0}^{2\pi} L_i' \cos\theta' \rho_e \ell(\theta',\psi';\theta,\psi) \sin\theta' d\theta' d\psi' \qquad (A13)$$

and the total flux Φ_i reaching the detector is

$$\Phi_i = \Delta\omega \Delta A \cos\theta \int_{\theta'=0}^{\pi/2} \int_{\psi'=0}^{2\pi} L_i' \rho_e \ell(\theta',\psi';\theta,\psi) \cos\theta' \sin\theta' d\theta' d\psi' \qquad (A14)$$

where $\Delta\omega$ is the solid angle subtended by the detector from the specimen and θ, ψ is the direction of the detector. O_i again is $\Phi_i R$.

When the specimen is replaced by a mirror standard of reflectance ρ_s, figure 2B, the incident beam coming from a solid angle $\Delta\omega''$ centered about the direction θ'', ψ'', where $\theta'' = \theta$ and $\psi'' = \psi + \pi$, will be specularly reflected by the standard to the detector. All flux incident on the standard from other directions will be reflected away from the detector. The flux Φ_{is} incident on the detector is

$$\Phi_{is} = L_i' \rho_e \rho_s \Delta A'' \cos\theta'' \Delta\omega \qquad (A15)$$

and the signal from the detector, O_{is}, is $\Phi_{is} R$.

$$\frac{O_i}{O_{is}} = \frac{R\Delta\omega\Delta A \cos\theta \int_{\theta'=0}^{\pi/2} \int_{\psi'=0}^{2\pi} L_i' \rho_e \ell(\theta',\psi';\theta,\psi) \cos\theta' \sin\theta' d\theta' d\psi'}{R L_i' \rho_e \rho_s \Delta A'' \cos\theta'' \Delta\omega} \qquad (A16)$$

but $\Delta\omega''$ is the mirror reflection of $\Delta\omega$, and hence $\Delta A \cos\theta = \Delta A'' \cos\theta''$, and

$$\frac{O_i}{O_{is}} = \frac{1}{\rho_s} \int_{\theta'=0}^{\pi/2} \int_{\psi'=0}^{2\pi} \ell(\theta',\psi';\theta,\psi) \cos\theta' \sin\theta' d\theta' d\psi' \qquad (A17)$$

But $\ell(\theta,\psi;\theta;\psi') = \ell(\theta',\psi';\theta,\psi)$, hence equation (A17) is equivalent to equation (A9) and the emr measures a quantity having the same numerical value when used in direct and inverse modes, if flux losses are neglected.

The flux ratio measured in the inverse mode is $R(2\pi;\theta',\psi')/\rho_s$. $R(2\pi;\theta',\psi')$ is the hemispherical-directional reflectance factor. Judd [17] defines reflectance factor as follows:

"Reflectance factor (at a point on a surface, for the part of the reflected radiation contained in a given cone, and for incident radiation of given spectral and geometric distributions): Ratio of the radiant flux reflected in the directions delimited by the cone to that reflected in the same directions by a perfectly reflecting diffuser, identically irradiated."

The modifier "hemispherical" defines the geometric conditions of irradiation as being uniform over a hemisphere, and the modifier "directional" defines the cone of reflected radiant flux accepted for measurement as being of small solid angle about a given direction.

From the above definition

$$R(2\pi;\theta,\psi) \equiv \frac{\int_{\theta'=0}^{\pi/2}\int_{\psi'=0}^{2\pi} L_i' \Delta A \cos\theta \Delta\omega \ell(\theta',\psi';\theta,\psi) \sin\theta' \cos\theta' d\theta' d\psi'}{L_i \Delta A \cos\theta \Delta\omega}$$

and for a completely reflecting, perfectly diffusing surface,

$L_i' = L_i$ (since $\Phi_i' = \Phi_i$, or $\Delta A \pi L_i' = \Delta A \pi L_i$), hence

$$R(2\pi;\theta,\psi) \equiv \int_{\theta'=0}^{\pi/2}\int_{\psi'=0}^{2\pi} \ell(\theta',\psi';\theta,\psi) \sin\theta' \cos\theta' d\theta' d\psi'$$

$$\equiv \int_{\theta'=0}^{\pi/2}\int_{\psi'=0}^{2\pi} \ell(\theta,\psi;\theta',\psi') \sin\theta' \cos\theta' d\theta' d\psi'$$

$$\equiv \rho(\theta,\psi;2\pi) \ .$$

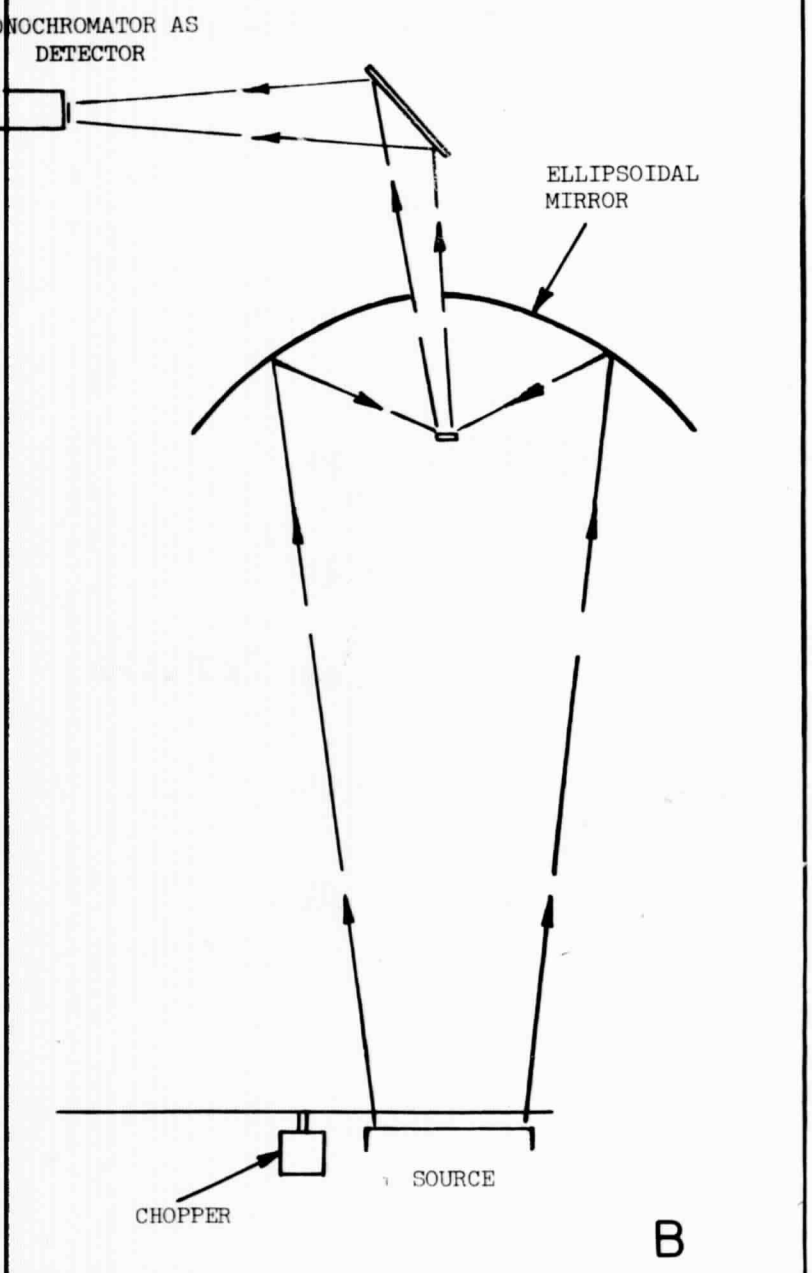

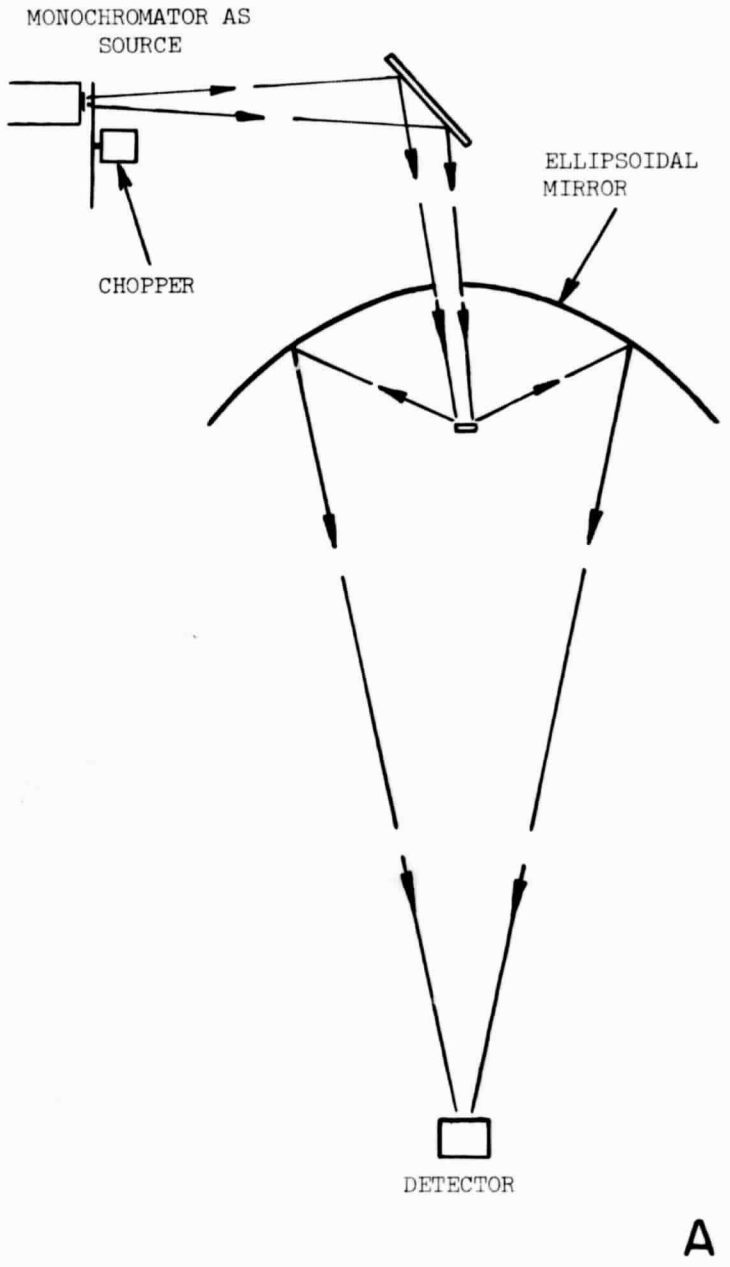

Figure 1. Schematic diagrams of ellipsoidal mirror reflectometer. A - direct mode. B - inverse mode.

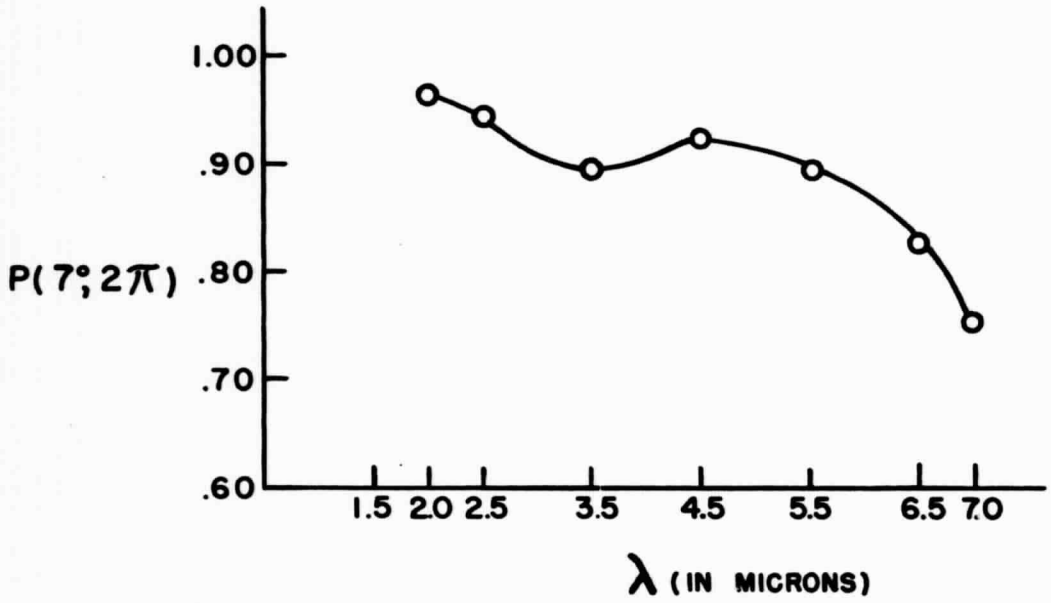

Figure 2.

Spectral directional-hemispherical reflectance of mu sulfur.

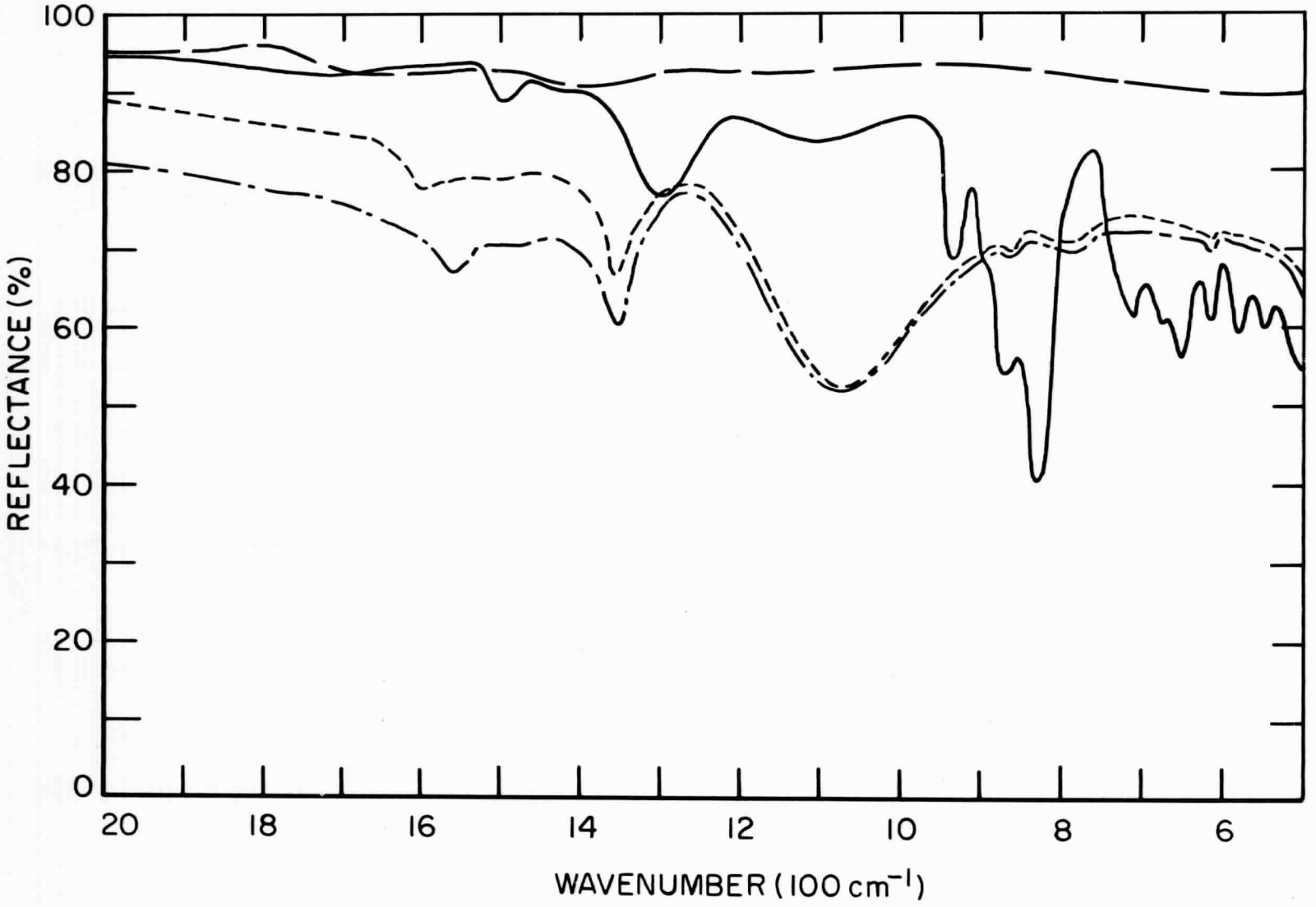

Figure 3.

Spectral directional-hemispherical reflectance of cesium iodide powder.

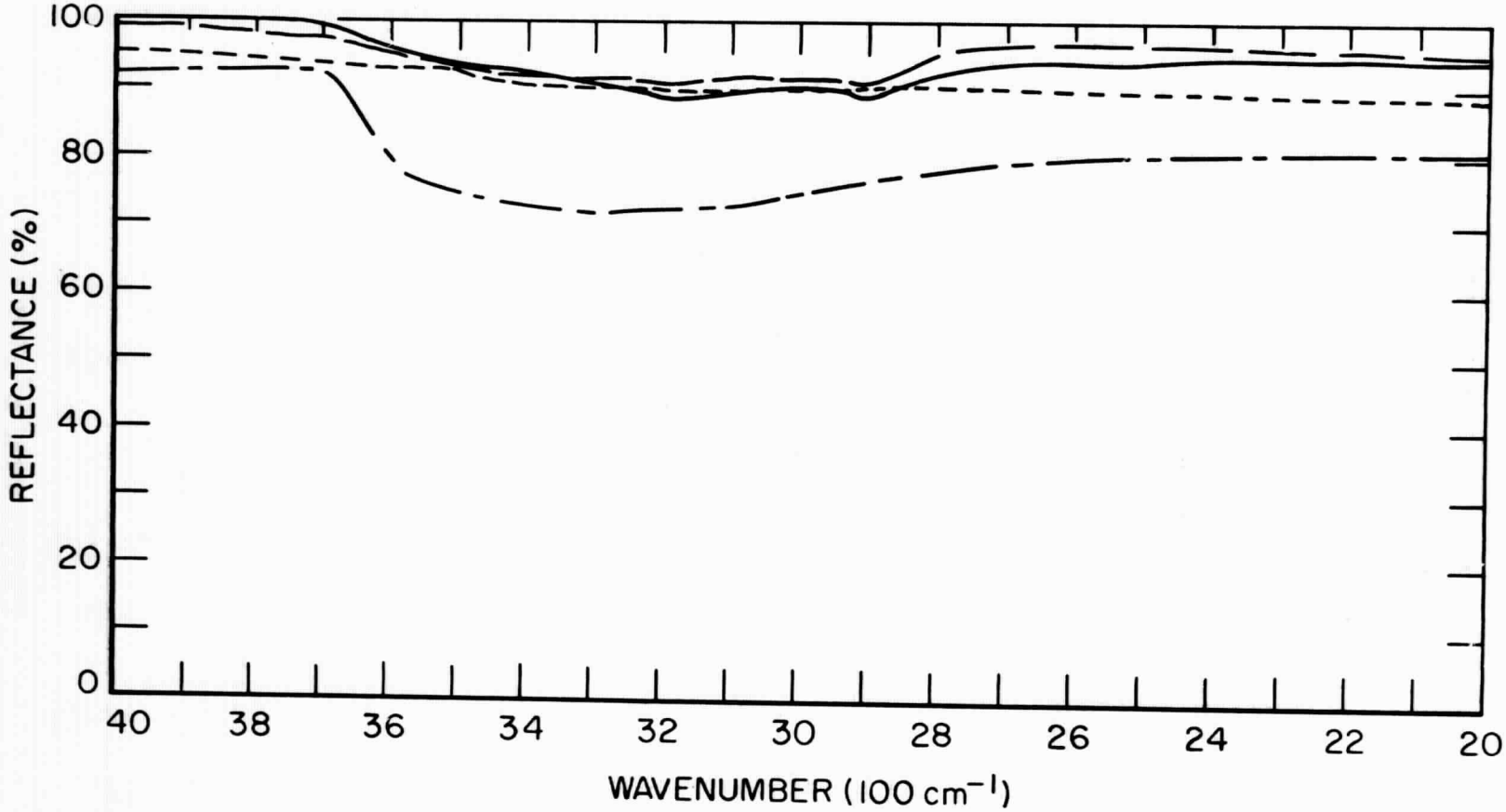

Figure 4.

Spectral directional-hemispherical reflectance of cesium iodide powder.

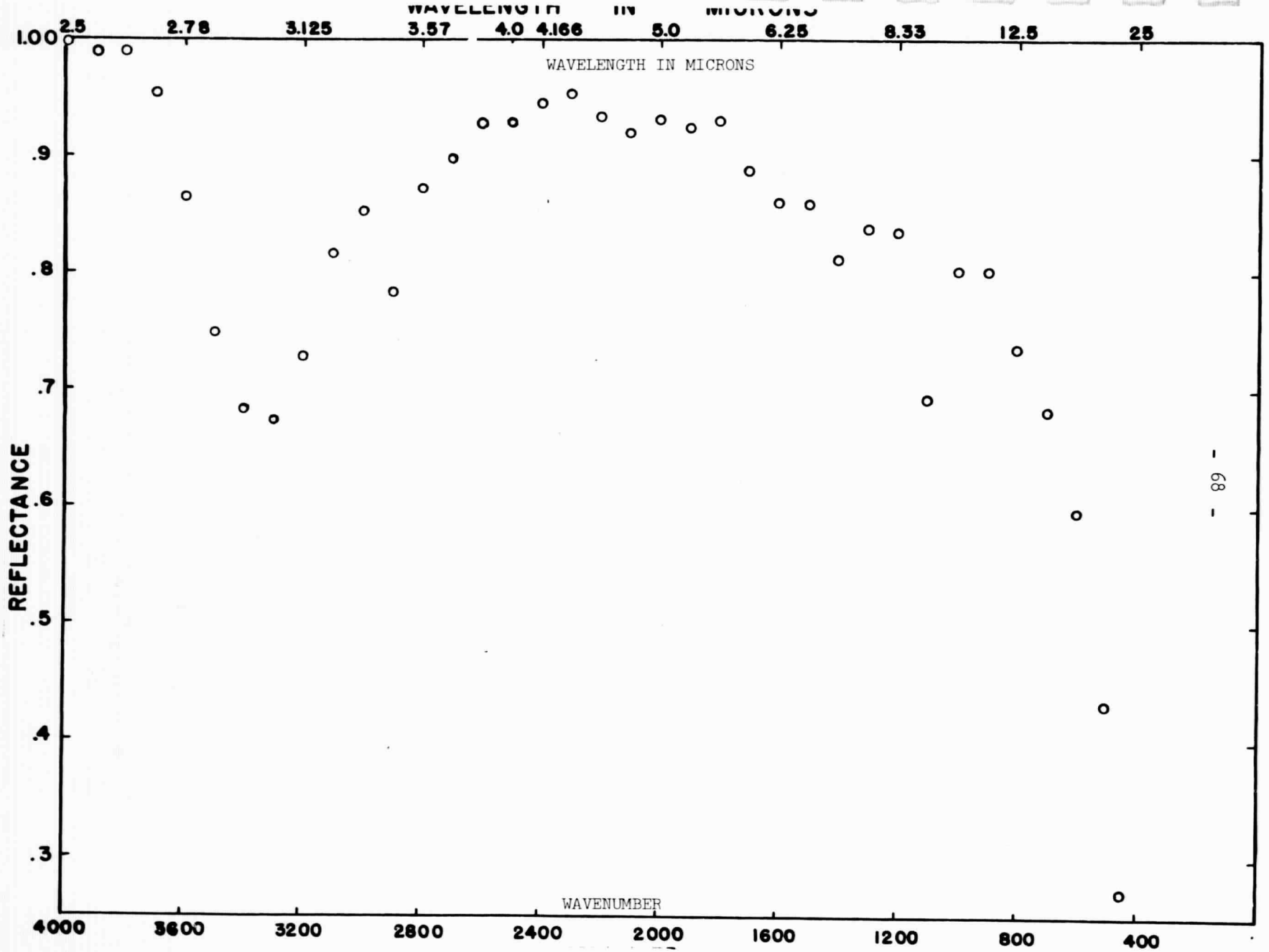

Figure 5. Spectral directional-hemispherical reflectance of a sprayed sodium chloride coating.

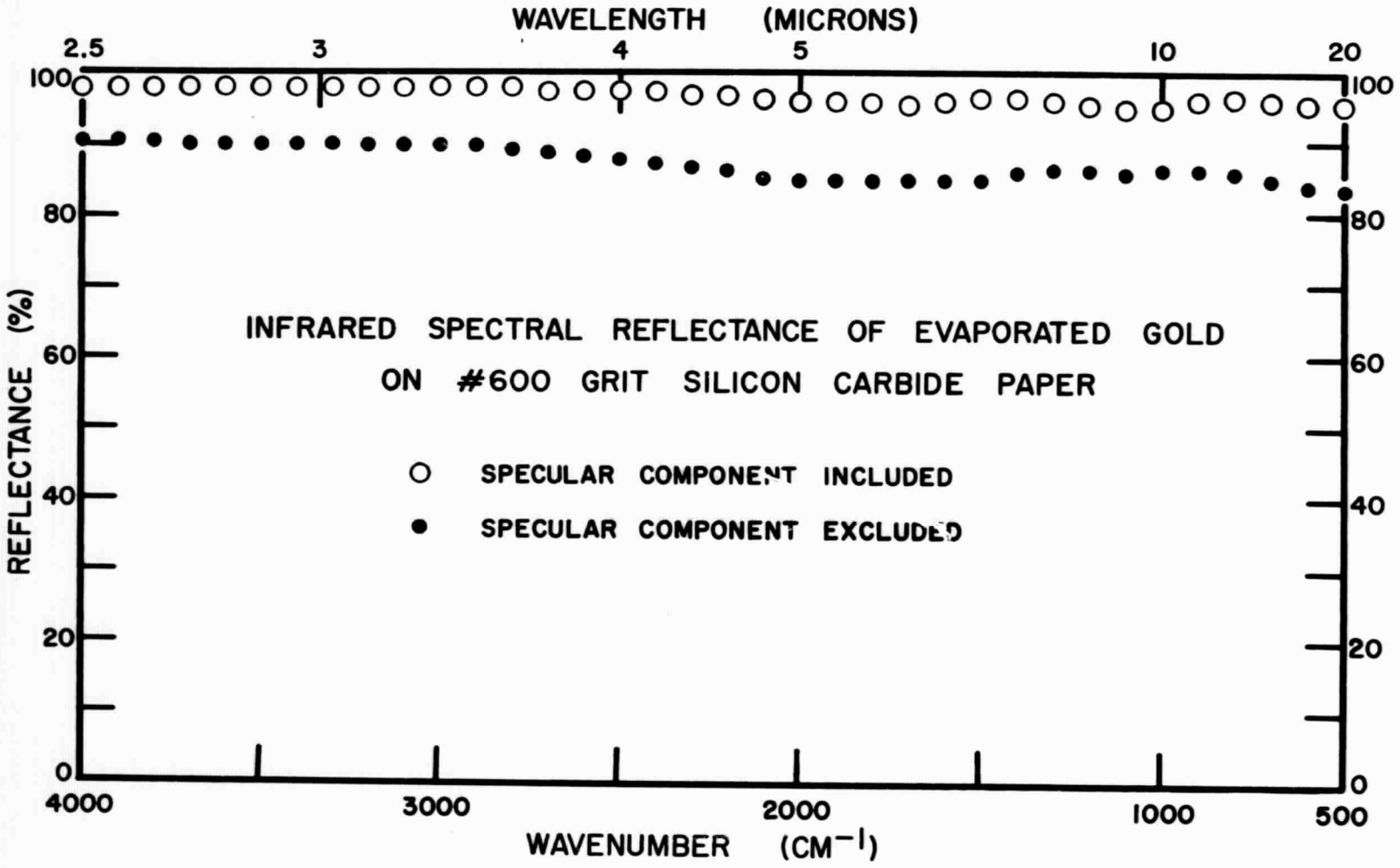

Figure 6.

Spectral directional-hemispherical reflectance of gold-coated No. 600 silicon carbide polishing paper.

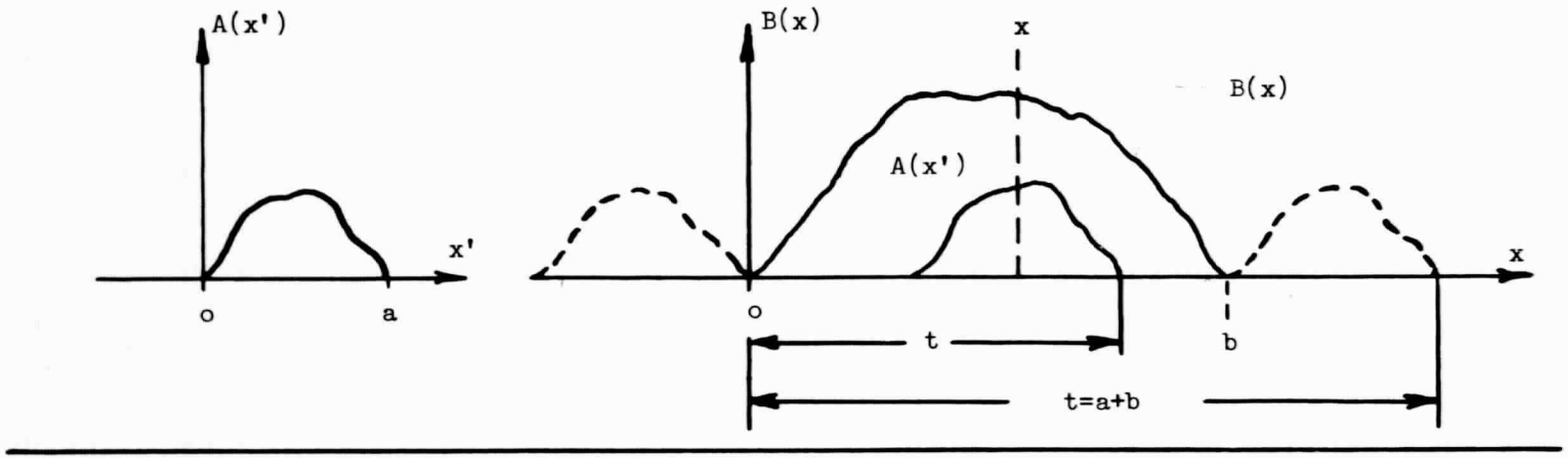

$A(x') = 0$ outside $(o;a)$

$B(x) = 0$ outside $(o;b)$

Figure 7.

Parameters used in deriving scanning equations.

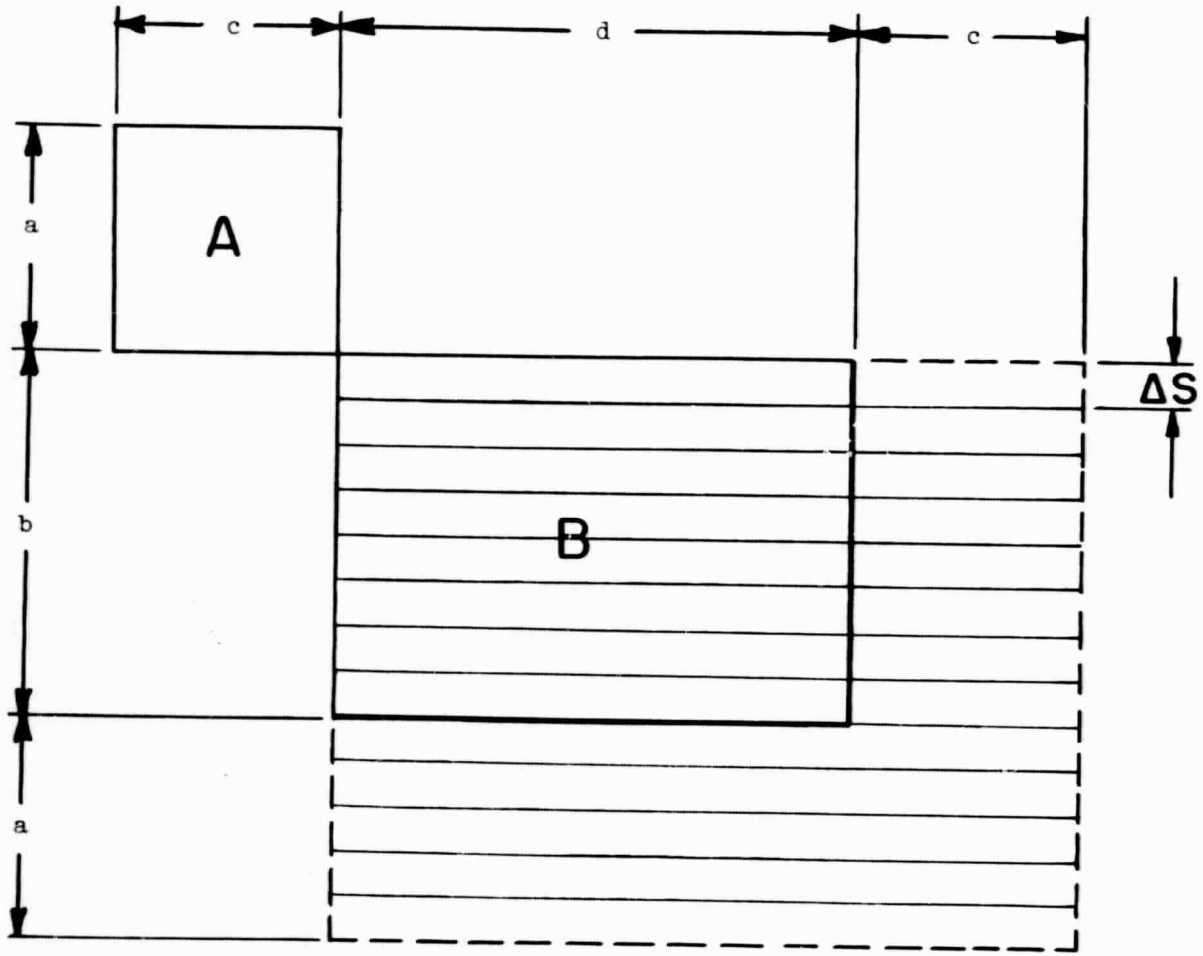

Figure 8.

Ideal raster pattern for scanning.

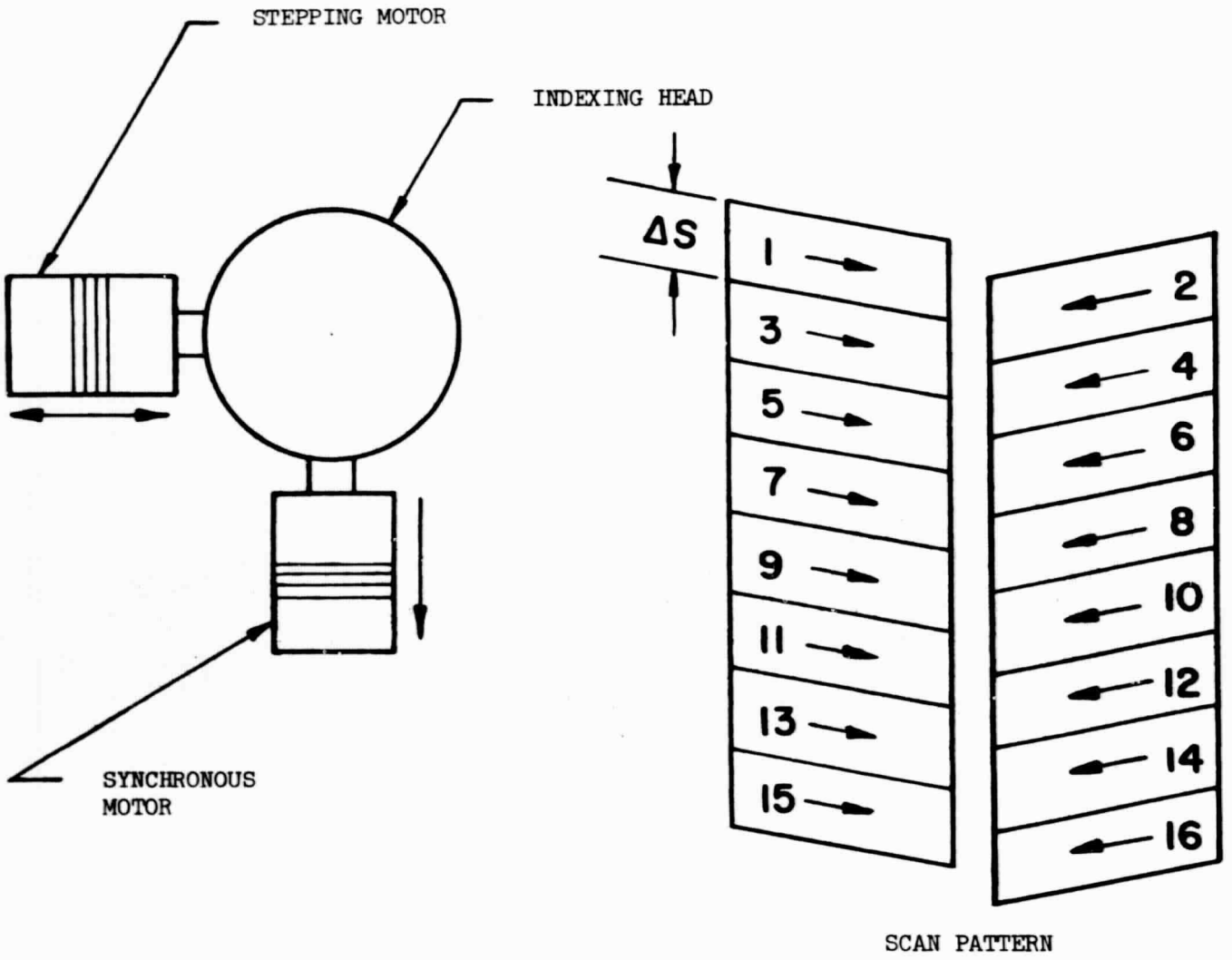

Figure 9.

Schematic of scanning system and pattern produced.
The two scan patterns are superimposed.

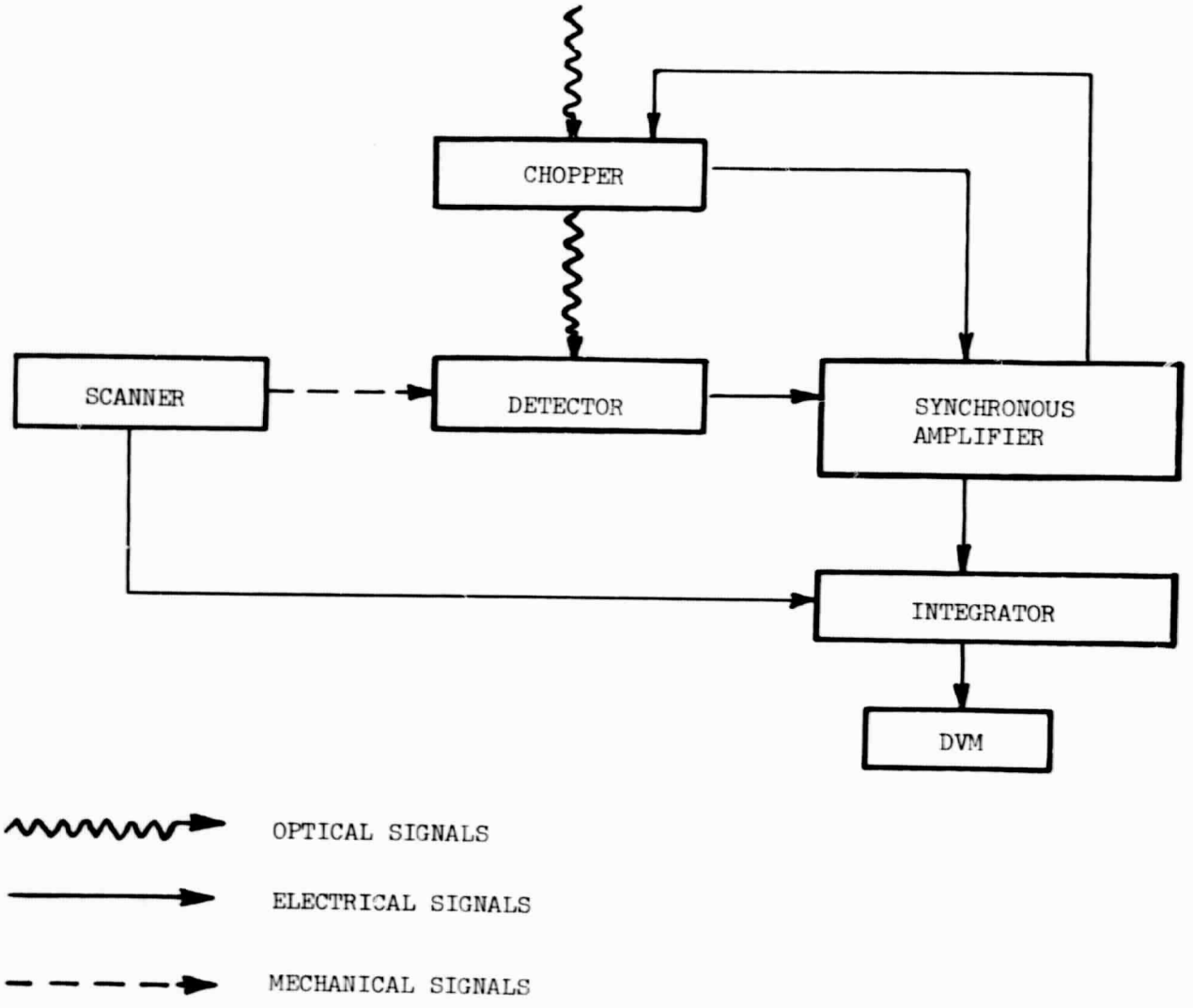

Figure 10.

Block diagram of signal processing system used with scanner.

TEST OF INTEGRATOR

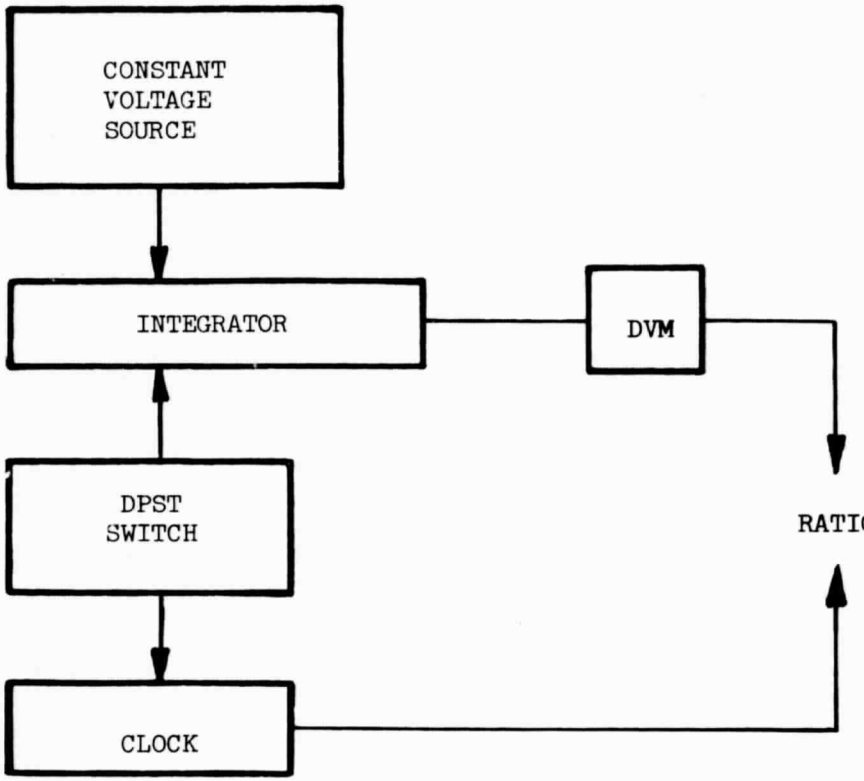

	RATIO
	.52964
	.52976
	.52983
	.52988
	.52985
	.52968
	.52980
	.52971
AVG	.52977

MAX % DEVIATION .02%

Figure 11.

Block diagram of equipment used to test reproducibility of integrator, and results obtained.

TEST OF AMPLIFIER AND DETECTOR

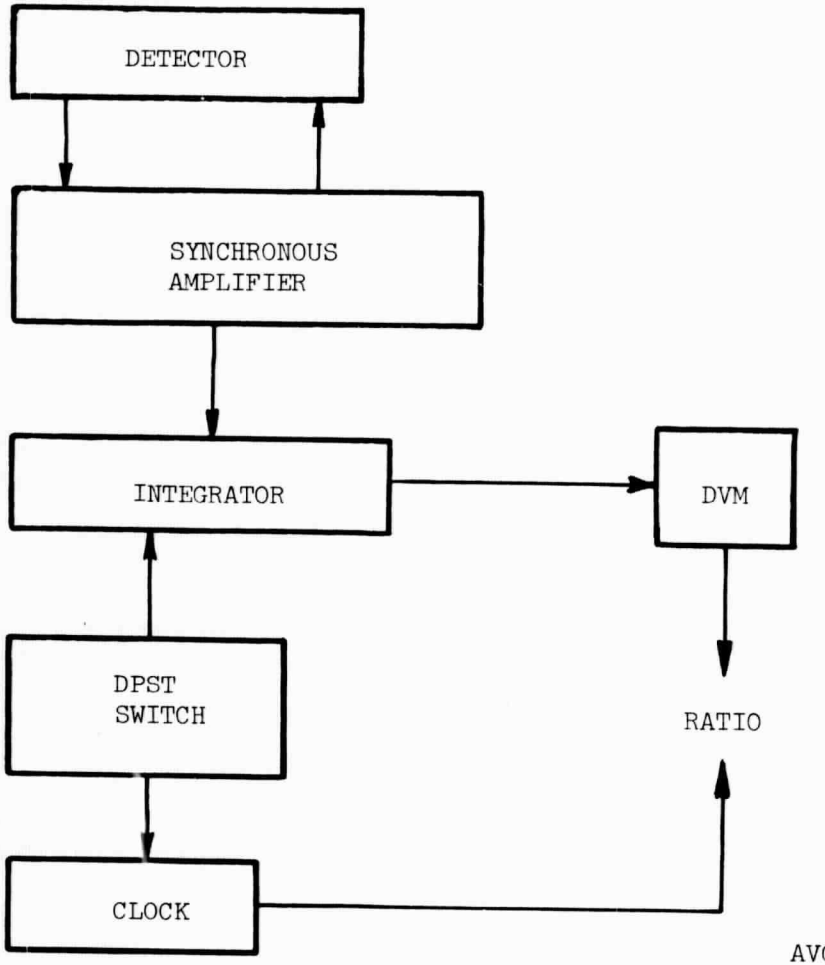

	RATIO	
	1.0666	3 MINUTES
	1.0664	
	1.0677	
	°	6 MINUTES
	°	
	°	
	1.0668	
	1.0673	
	1.0668	
	°	
	°	
	°	
	1.0670	
	1.0690	
	1.0662	
	°	
	°	
	°	
	1.0680	
	1.0660	
	1.0669	
AVG.	1.0671	
MAX % DEV.	.18%	

Figure 12.

Block diagram of equipment used to test reproducibility of amplifier and detector, and results obtained.

TEST OF SCANNER

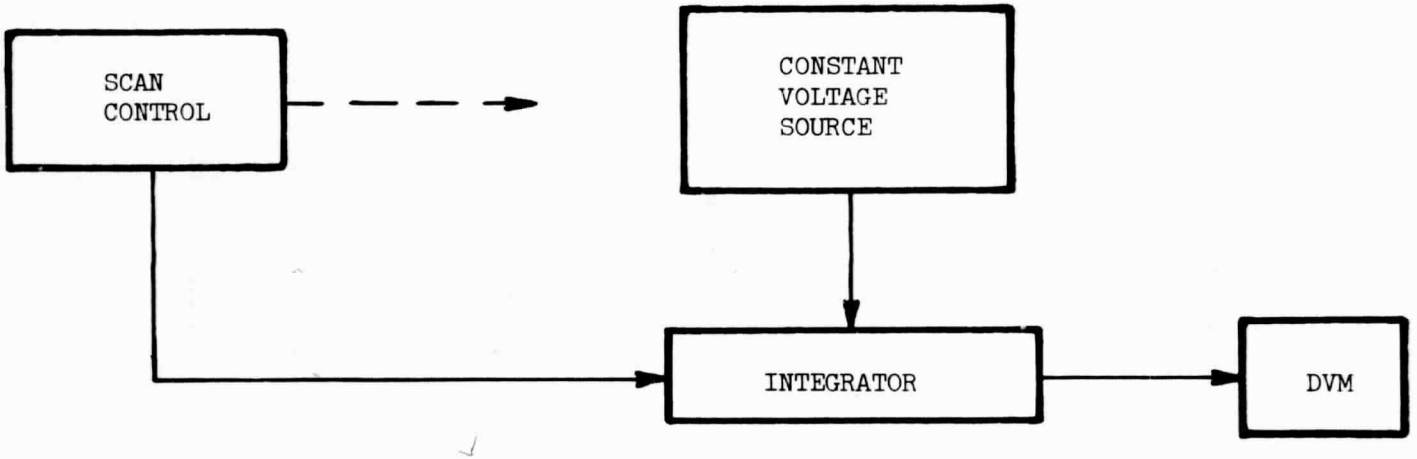

Data (8 minutes between starts of each 7 minute scanning period, 1 hour between groups)

	#1	#2	#3
	1.898	1.896	1.897
	1.897	1.895	1.896
	1.896	1.895	1.895
	1.896	1.895	1.894
	1.896	1.895	1.894
AVG	1.8966	1.8952	1.8952
MAX % DEVIATION	.07%	.04%	.09%

Figure 13.

Block diagram of equipment used to test reproducibility of scanner, and results obtained.

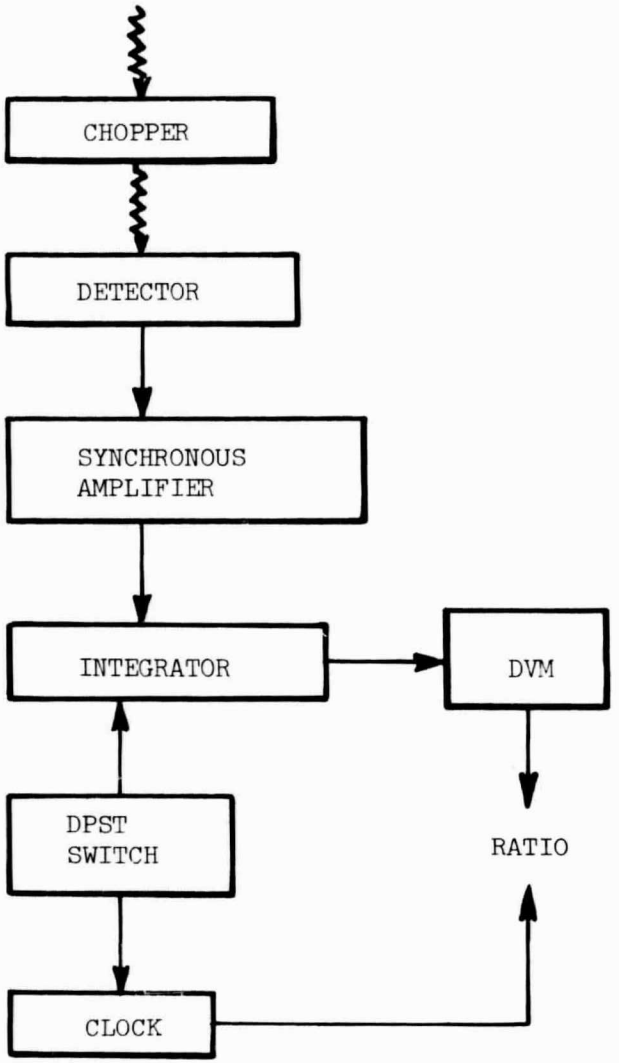

	RATIO	
	1.3870	
	1.3880	
	1.3894	
	1.3966	
	1.3927	
	1.3900	
	1.3924	20 minutes
	1.3938	
	1.3941	
	1.3931	
	1.3938	
	1.3935	
	1.3936	
AVG.	1.3921	
MAX % DEV.	.36%	
	1.3823	100 minutes later
	1.3856	
MAX % DEV.	.7%	

Figure 14.

Block diagram of equipment used to test reproducibility of Globar source, and results obtained.

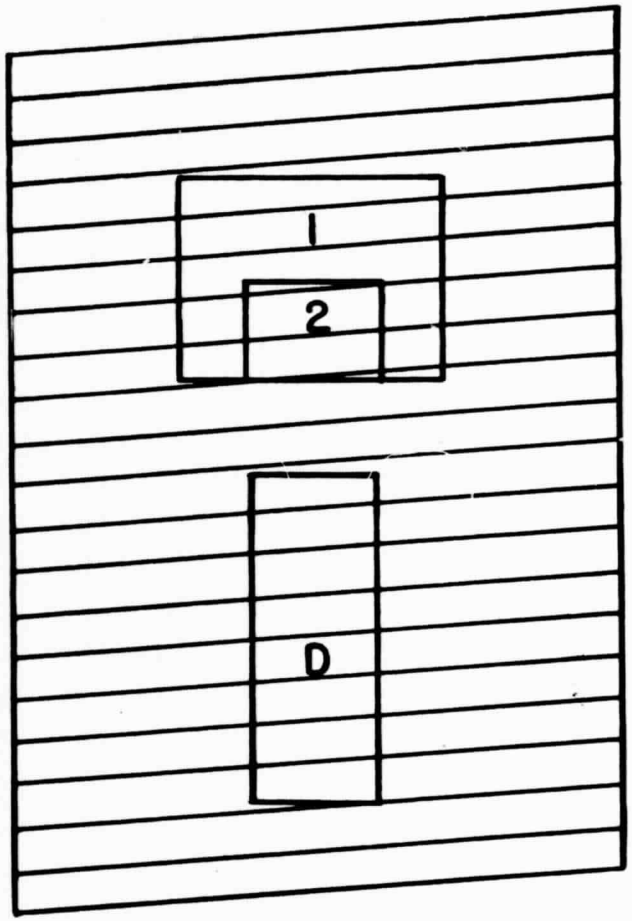

	1	2
	1.072	1.075
	1.064	1.084
	1.075	1.078
AVG.	1.0703	1.0790

Δ AVG = .0087 ± .0088

at 95% level

Figure 15.

Sketch showing relative size of scan pattern, images (1 and 2) and detector, and results obtained.

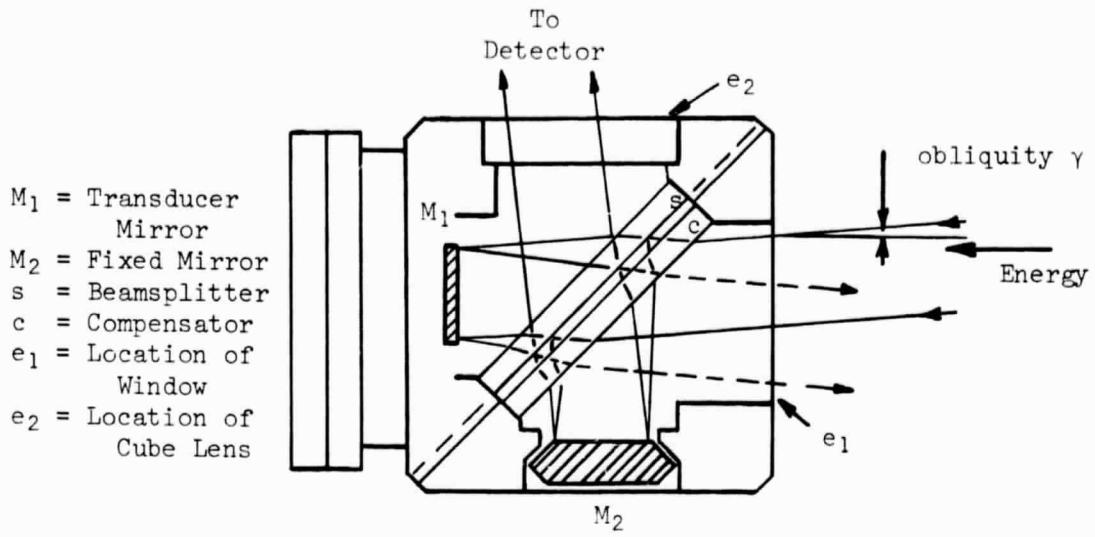

Figure 16.

Cross-sectional drawing of interferometer head.
M_1 is the movable mirror, M_2 the fixed mirror, S the beamsplitter, C the compensator plate, e_1 the entrance aperture and e_2 the exit aperture.

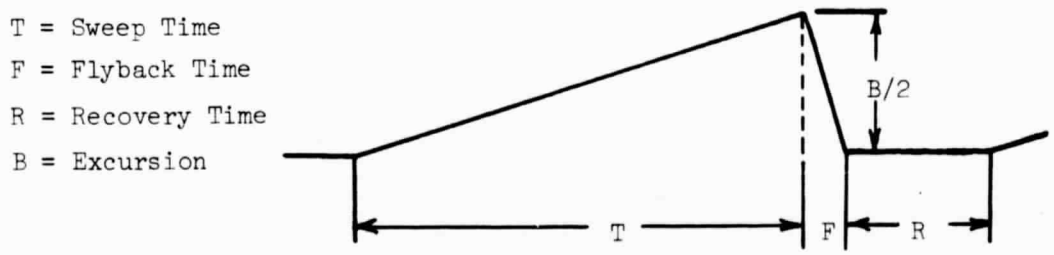

Figure 17.

Plot of mirror motion during a sweep.
T is sweep time, F is fly-back time, R is recovery time and B/2 is excursion, or maximum distance of travel of the mirror.

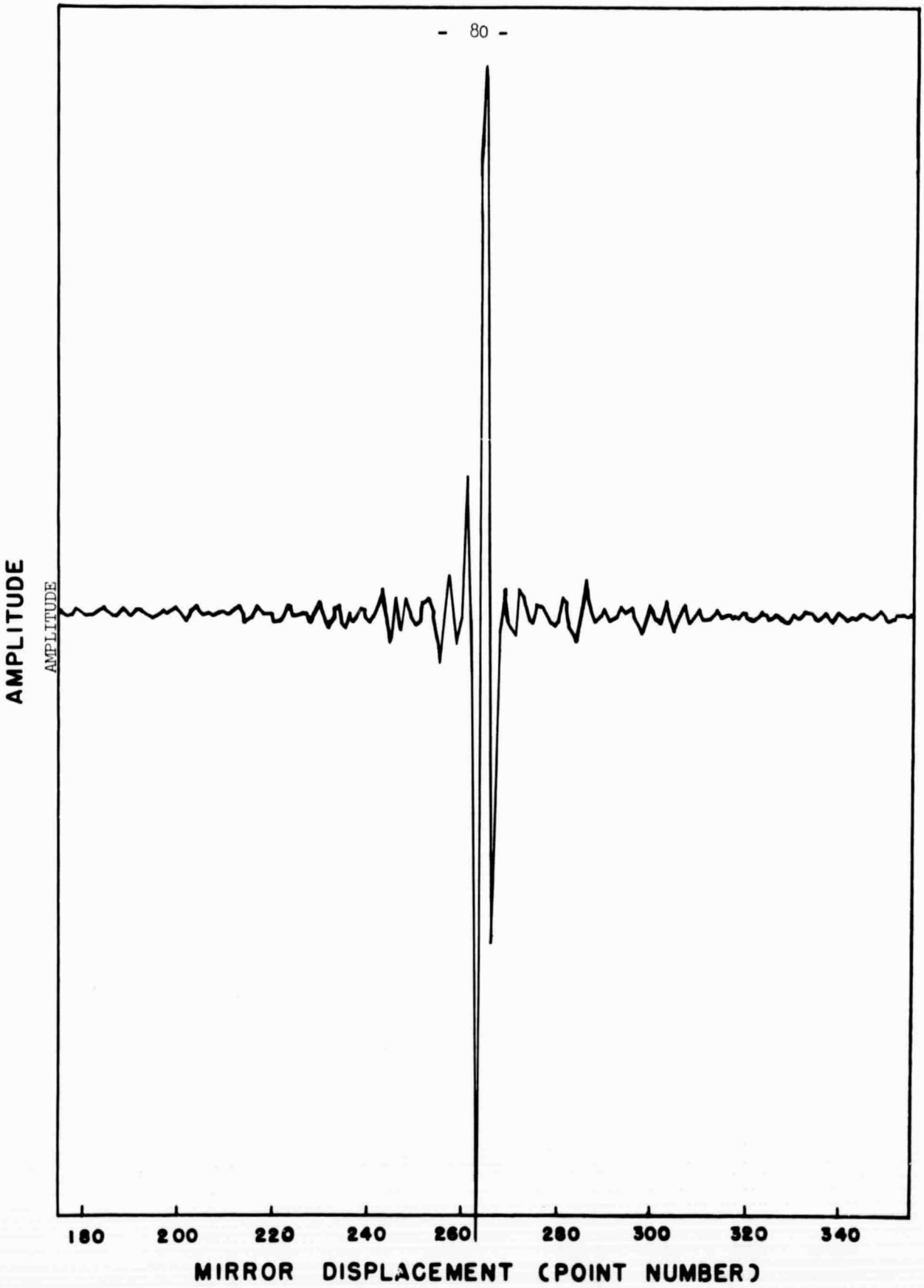

Figure 18. A typical interferogram for a polychromatic beam.
Only the central 180 points of the 521 recorded are included on this plot.

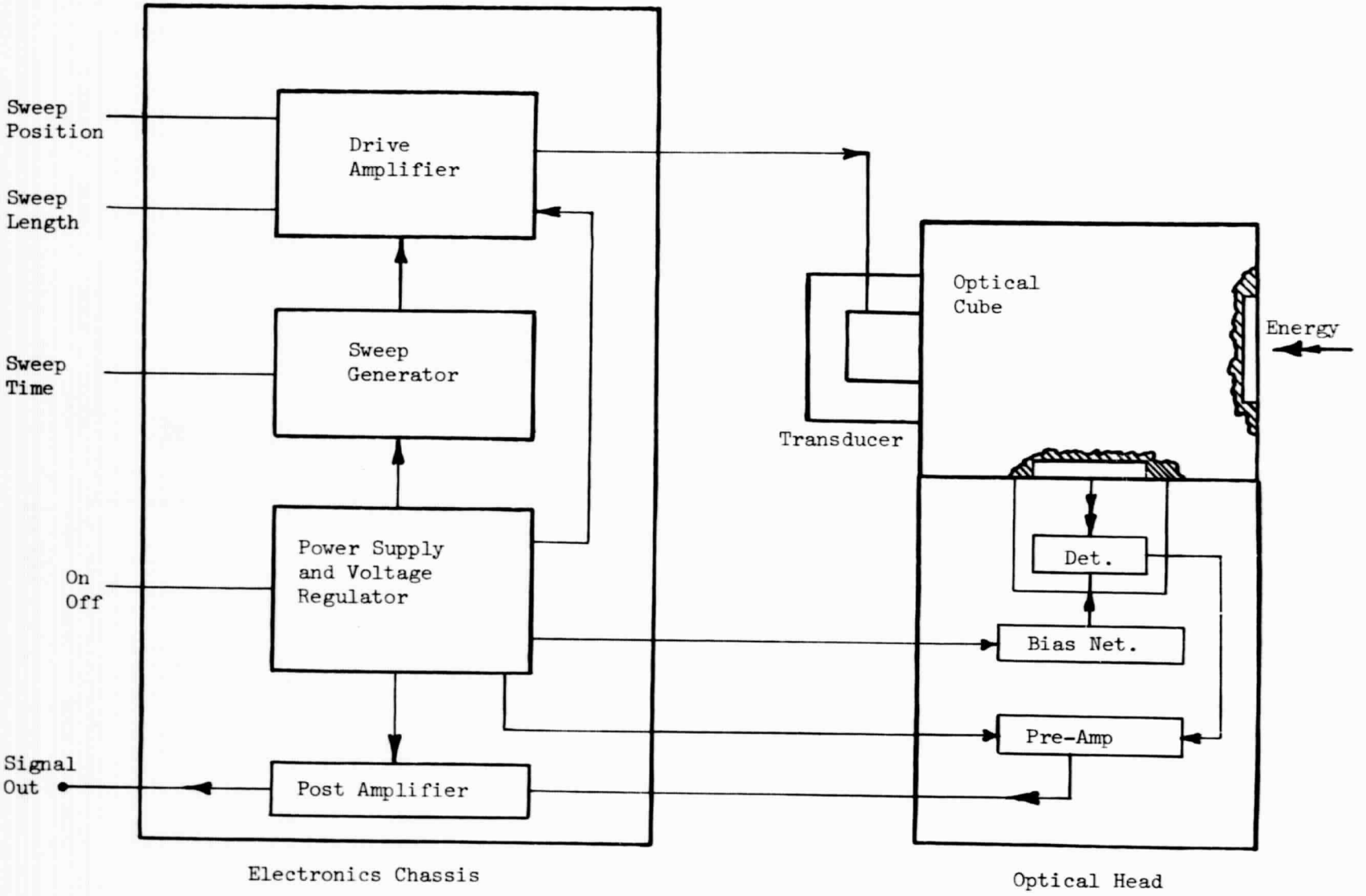

Figure 19.

Block diagram of the electronic system of the interferometer spectrometer.

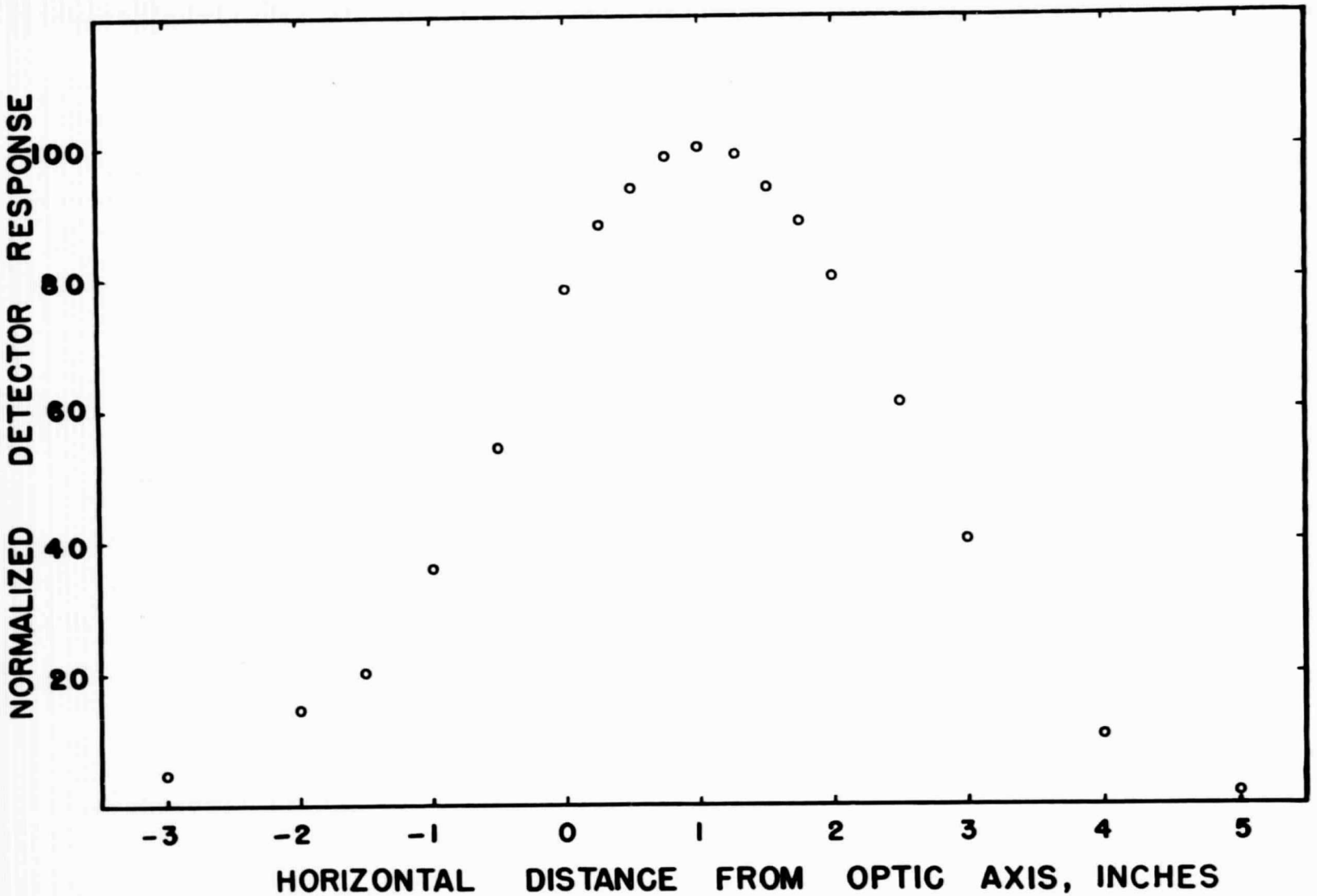

Figure 20. Normalized detector response as a function of detector position along a horizontal line through the optical axis 28 inches from the interferometer-source combination. Distances are in inches, with positive distances to the right and negative distances to the left of the optical axis, facing the interferometer.

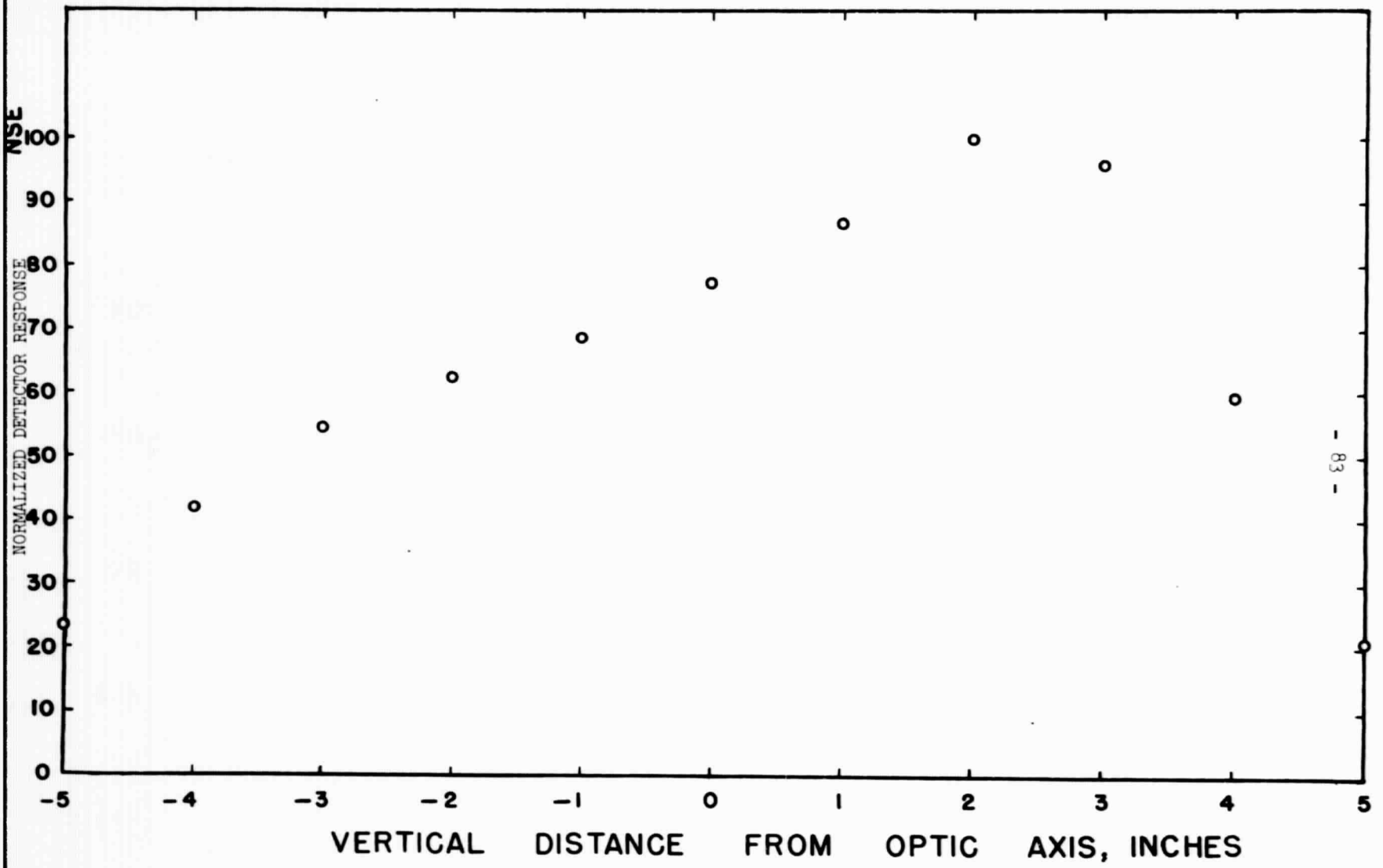

Figure 21. Normalized detector response as a function of detector position along a vertical line through the optical axis, 28 inches from the interferometer-source combination. Distances are in inches, with positive distances above and negative distances below the optical axis.

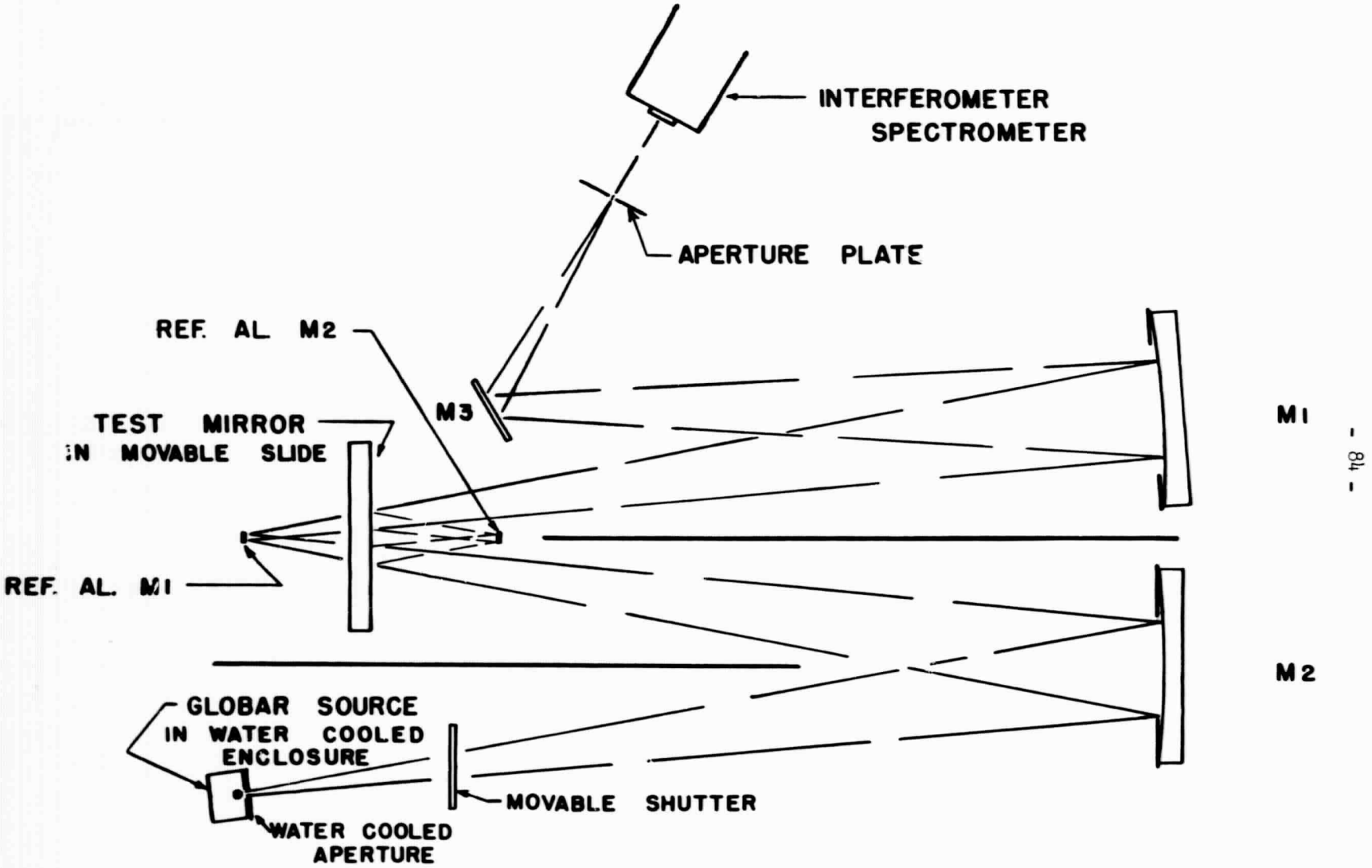

Figure 22.

Optical diagram of the Strong reflectometer used with the interferometer spectrometer.

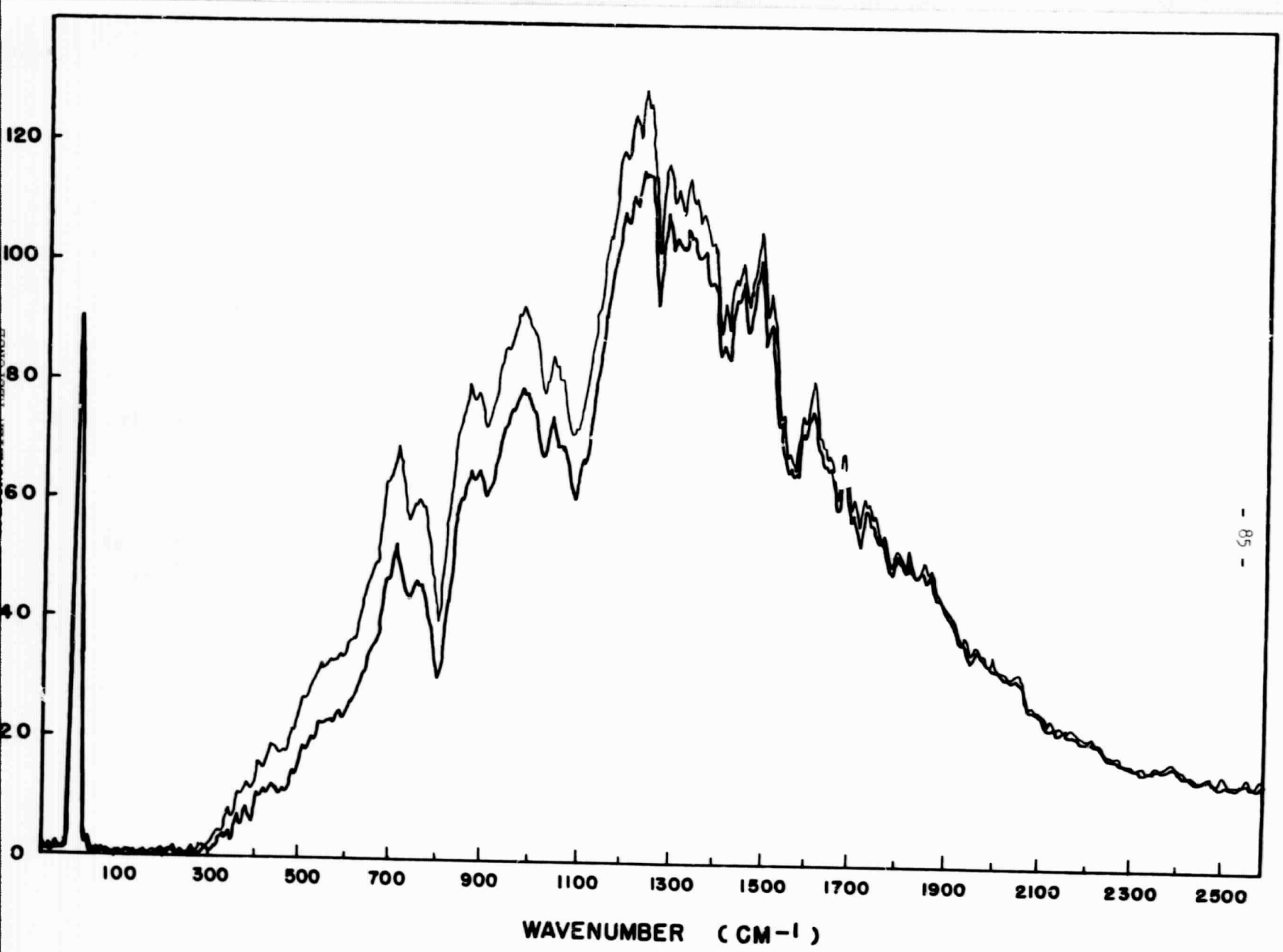

Figure 23. Typical curves produced by analog reduction of an interferogram recorded without background subtracted (lower curve) and with background subtracted (upper curve).

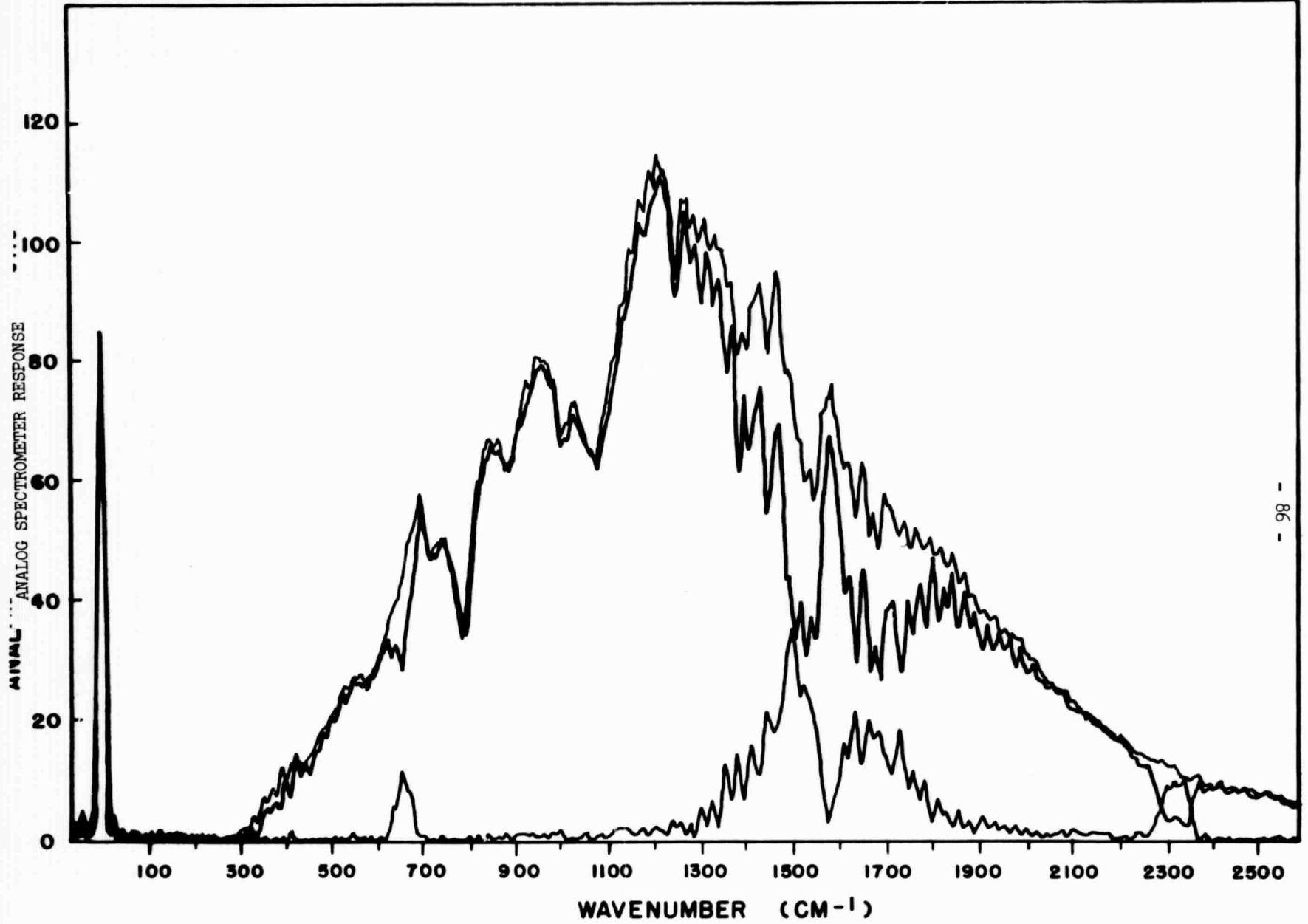

Figure 24. Typical spectrum produced by a Globar source in purified atmosphere (top curve) and ambient atmosphere (middle curve). The difference, bottom curve, represents the observed absorption of the ambient atmosphere.

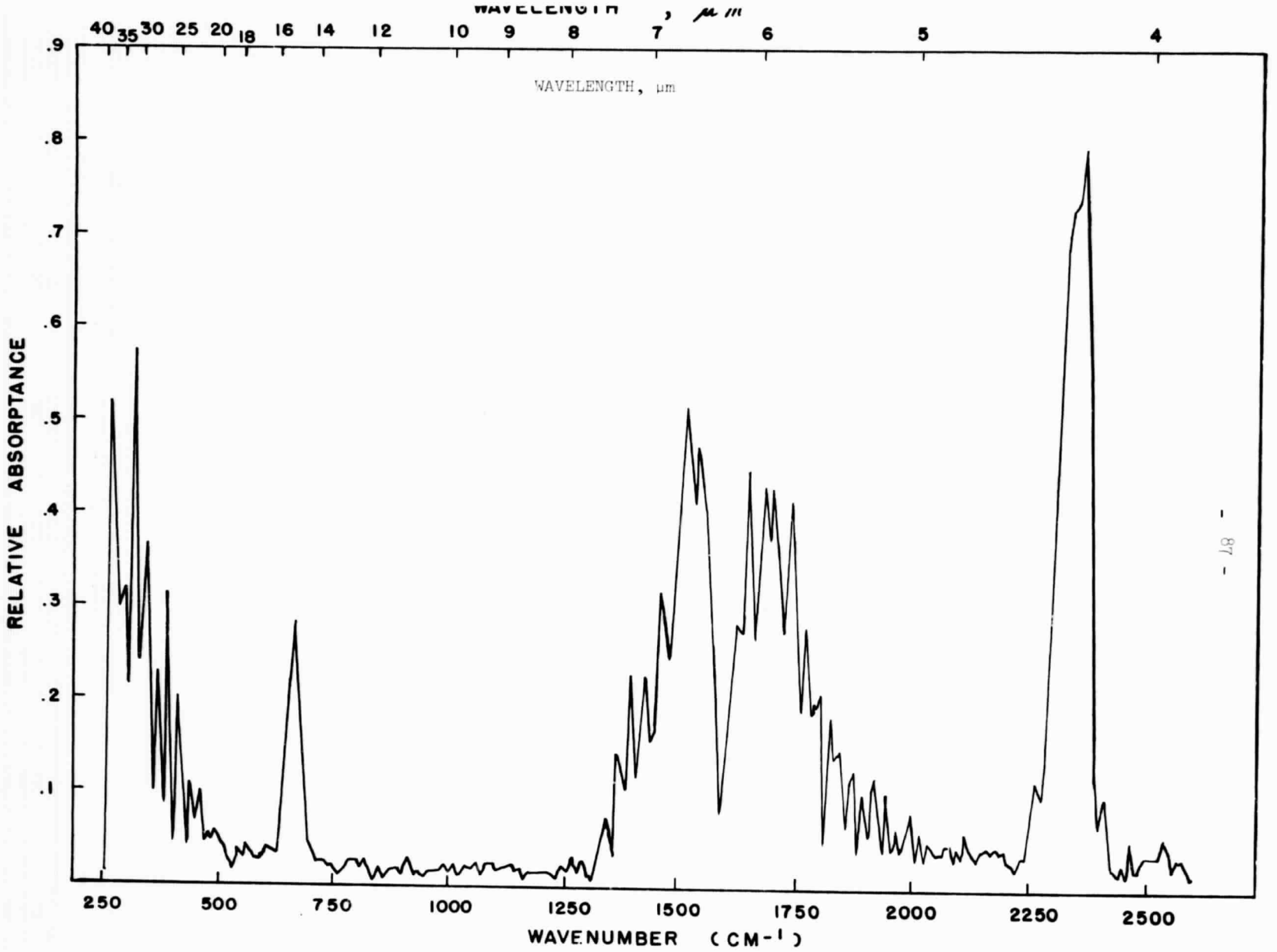

Figure 25. Typical spectral distribution of observed atmospheric absorptance, obtained by digital reduction of interferograms. Each point is the ratio of the difference in observed spectral radiances of the Globar source observed in purified and ambient atmospheres to that in the purified atmosphere.

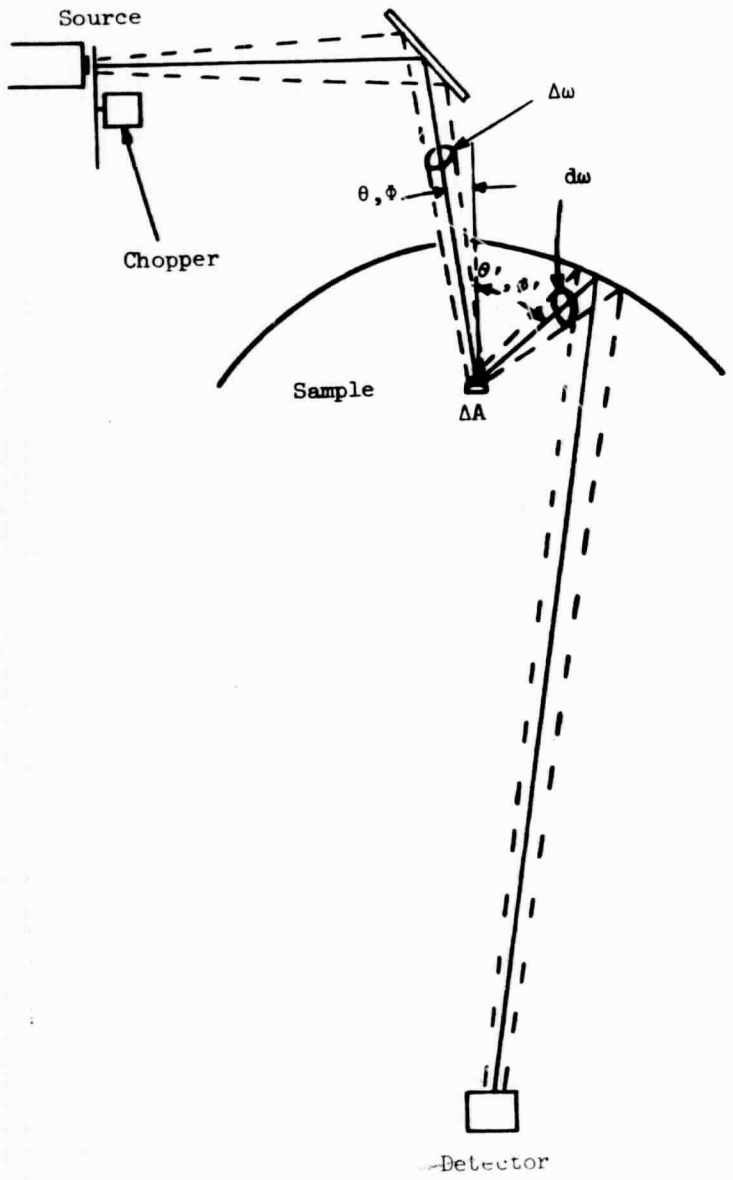

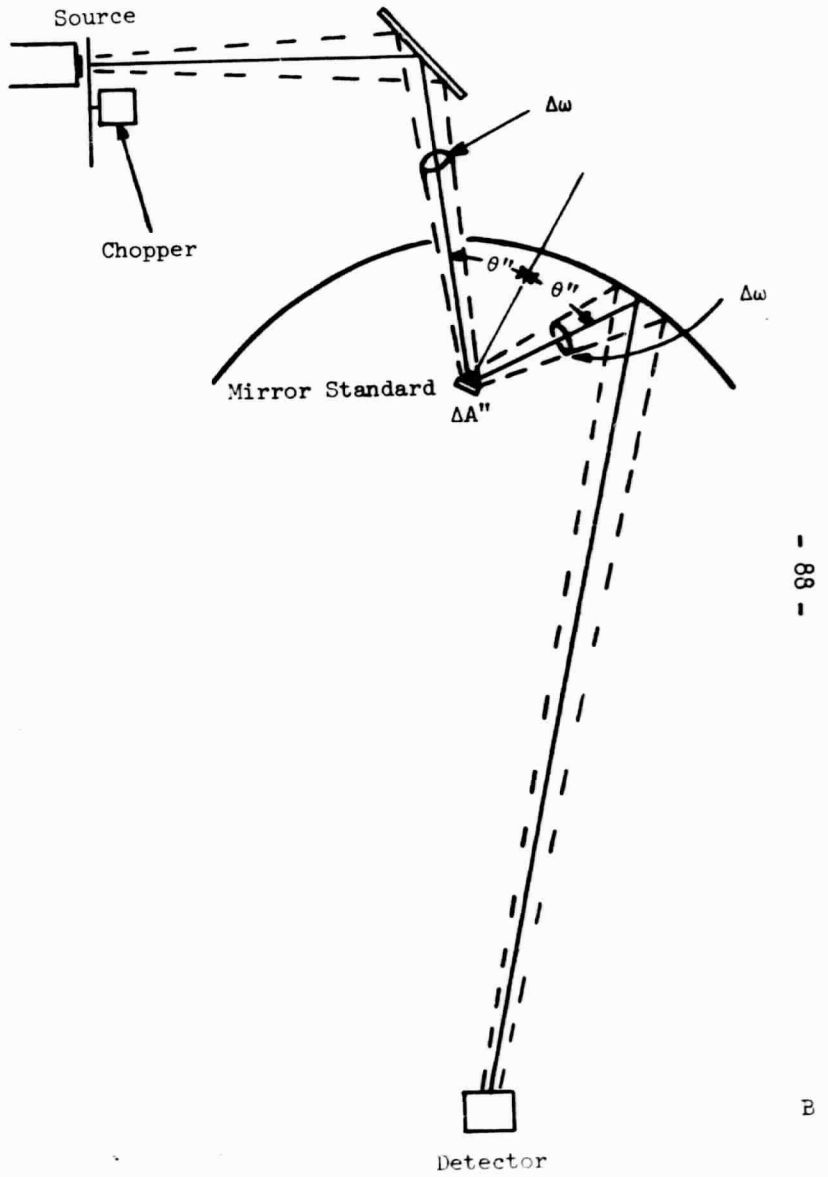

Figure A1. Ellipsoidal mirror reflectometer in direct mode, showing parameters used in equations A3 through A5.

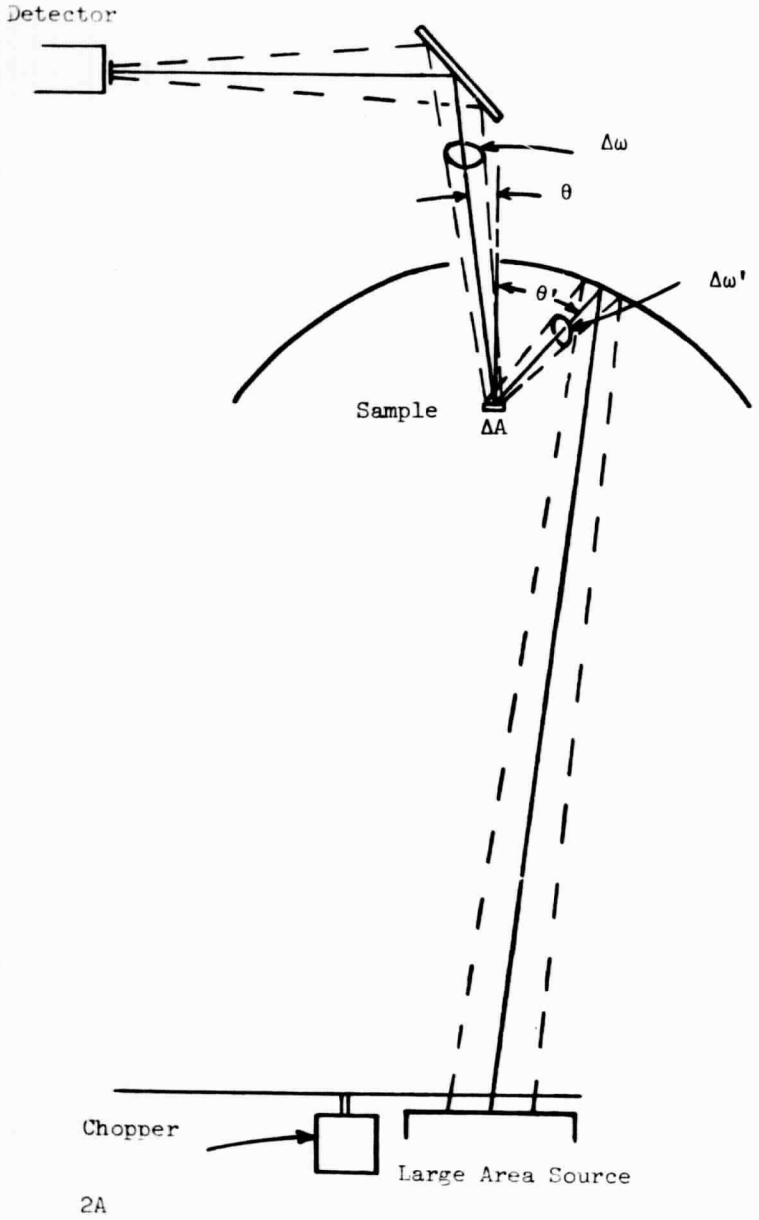

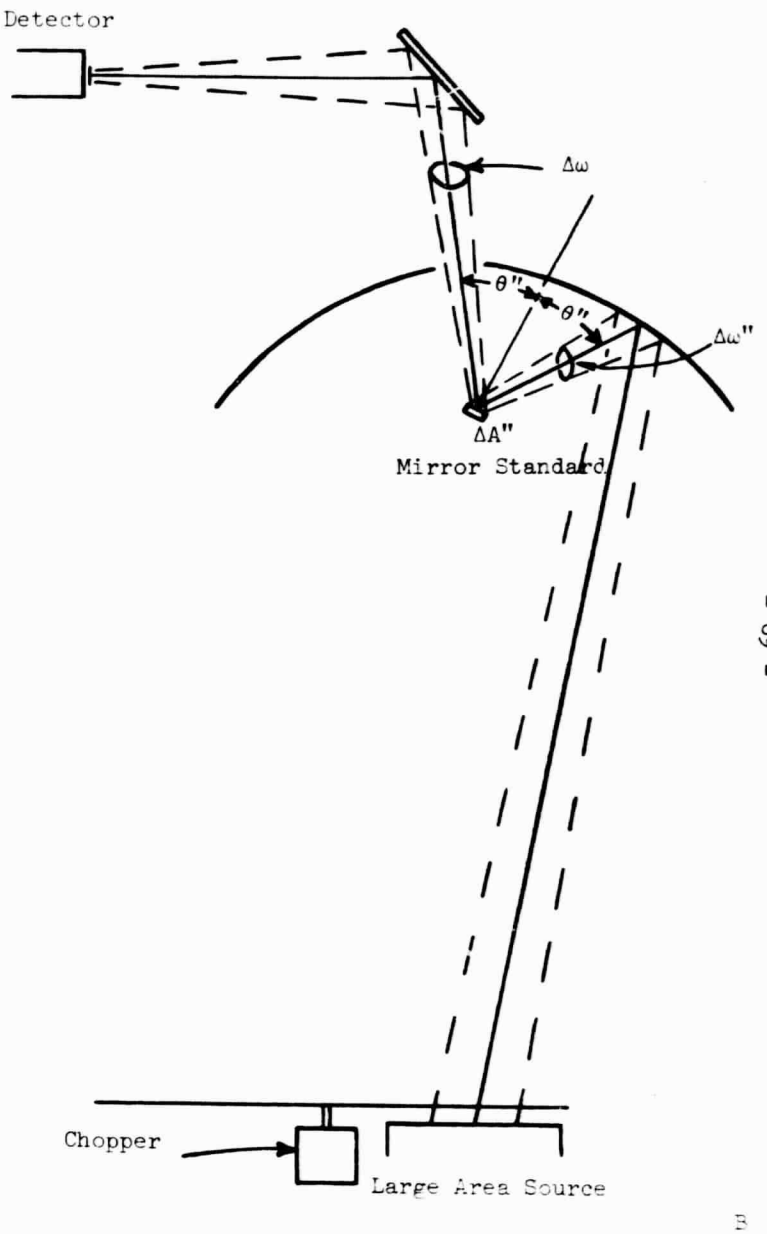

Figure A2. Ellipsoidal mirror reflectometer in inverse mode, showing parameters used in equations A11 through A16.